

Sensitivity in MALDI MS with small spot sizes

by

ANDRIY YAMCHUK

A Thesis submitted to the Faculty of Graduate Studies of
The University of Manitoba
in partial fulfilment of the requirements of the degree of

MASTER OF SCIENCE

Department of Physics and Astronomy
University of Manitoba
Winnipeg, Manitoba, Canada

Copyright ©2013 by Andriy Yamchuk

Abstract

In MALDI, for laser fluences below the saturation point the ion yield per shot follows a cubic dependence on the irradiated area, leading to a conclusion that smaller spots produce overall less ions and therefore are less viable. However, Qiao *et al.* showed that by decreasing the laser spot size it is possible to raise the saturation point, and thus increase the ion yield per unit area, also known as sensitivity. Here we explore laser spots below 10 μm diameter to determine whether they offer any practical advantage. We show that sensitivity is greater for a flat-top 3–4 μm spot than for a 10 μm spot. The sensitivity is greater for a Gaussian-like 3–5 μm spot than for flat-top 5–25 μm spots. We also report for the first time sensitivity versus theoretical fluence profile for a Gaussian-like beam focused to a spot of 3–5 μm .

Contents

1	Introduction	1
1.1	Mass Spectrometry of Biomolecules	1
1.2	Matrix-assisted laser desorption/ionization	9
1.3	Imaging Mass Spectrometry	14
1.4	Sensitivity in MALDI	16
2	Experimental	20
2.1	Mass Spectrometry	20
2.1.1	Ion source	21
2.1.2	Quadrupole ion optics	34
2.1.3	Mass analyser	36
2.1.4	Detection	37
2.2	Sample Preparation	38
2.2.1	Sample and matrix preparations	38
2.2.2	Deposition methods	41
2.3	Data acquisition and analysis	46
3	Results and Discussion	49
3.1	Fibre optics	50
3.2	Fibreless optics	53
3.3	Sensitivity profiling	55
3.4	General discussion	58

3.5 Conclusion	59
--------------------------	----

List of Figures

2.1	Orthogonal time-of-flight mass spectrometer with a custom quadrupole and an ion source sections	22
2.2	Two on-line optical configurations in use	23
2.3	Energy profile of the fibre beam.	24
2.4	Two off-line optical geometries used for testing	27
2.5	Not calibrated size comparison between burn marks and grid mesh	30
2.6	Reduced exposure of the fibre beam showcasing an unusual three-lobe structure.	31
2.7	Circular artifacts found around the burn marks	32
2.8	An ion source assembly	33
2.9	Two axial field configurations	35
2.10	Substance P spectra	39
2.11	Electrospray deposition system	41
2.12	Signal from $500 \times 500 \mu\text{m}^2$ squares	43
2.13	Relative size of the matrix crystals using one layer spotting technique with different organic solvents.	45
2.14	A schematic of the raster program and its microscope images	47
3.1	Total ion yield generated by scanning $310 \times 310 \mu\text{m}^2$ area with $10 \mu\text{m}$ and $3\text{--}4 \mu\text{m}$ laser spot	52
3.2	Comparison of sensitivity results for fibre and fibre-less optics	54
3.3	Sensitivity profiles for $50 \mu\text{m}$ fibre and $3\text{--}5 \mu\text{m}$ Gaussian-like spot	57

Acknowledgements

I would like to extend my thanks to the following people who played an important role before, during and after my thesis completion.

Dr. Oleg Krokhin, my first mentor, introduced me to the field of applied mass spectrometry almost eight years ago when he hired me as his summer student. Oleg allowed me to learn independently through trial and error, but was always available to help me out with an advice. He provided me with analytical challenges and food for thought. He carefully guided me through peptide preparation, separation and analysis. He taught me how to perform *de novo* sequencing and how to read mass spectra. He gave me the fundamental basics that allowed me to tackle challenges in my project. I could not have started my mass spectrometry journey without his involvement. For that, I am grateful.

Dr. Ken Standing, for supporting me at the beginning of my career as a summer student, and allowing me to contribute to some of the more interesting projects applied to the real world problems. Through his collaborations, I've understood the challenges of multinational teams working together and benefits such collaborations can have.

Dr. Werner Ens, my first physics professor at the University of Manitoba, and project supervisor. At first intimidating, it took me some time to understand that he is very approachable and friendly person. I would like to thank him for hiring me as his summer student, and eventually making Master of Science out of me. I admire his patience and his ability to solve seemingly any analytical or technical problem

without leaving his office. He is a true genius that can image the problem in his head and find out almost immediately what went wrong. He can also see things not immediately apparent. I would like to thank him for inspiring me for greater things. I wish his dog and his family to live long and prosper.

Gilles Roy, Dr. Vladimir Montero Collado, Vijanaka Fernando, Dr. Hui Qiao and Andrew Pankewycz all deserve a mention. Gilles helped me solve countless technical issues with my research. His hands on experience is invaluable and my research would not be possible without his coffee mug, his ideas, or his *What do you want!* He taught me how to use lathe and drill, how to tap holes and how to manufacture my own equipment from raw materials.

Vladimir was always there when there was an instrument problem. He is very warm and intelligent person. He taught me some of the more technical aspects of the mass spectrometer, and showed me how to change oil in roughing pumps without shutting them down. I wish his daughter to finally realize her talents and become, one day, a great artist.

Vijanaka visited us a couple of times, and taught me about electronics. His quiet nature and approachable personality was only matched by his skill in electronics and his ingenuity. The things he created during his short stay were practical and useful.

Hui, my predecessor, showed me how to operate, troubleshoot the instrument, and how to take it apart and put it back so it works again. I hope you finally re-unite with your family.

Thanks go to Andrew for helping me out with a re-designed ionization source, and for teaching me how to properly file.

I would like to thank Dr. Linda Donald for continuous entertainment (and cookies) she provided every time she stepped into our lab.

I would like to thank my friend Ryan Desautels for lending me his optics books and providing me with various topics of discussion, from current news to the meaning of life of a graduate student; for involving me in Dungeons and Dragons and sparking

a love for board games.

Special thanks go to Susan Beshta, a graduate student liaison, for taking care of all the administrative details and calming me down during some of the desperate times.

Last, but not least, my family. My mom and dad, and my brother, who never lost faith in my long journey. Some of the best discussions were happening behind the scenes outside of the lab, inside their home. Thank you very much for supporting me during this interesting period of my life.

This research would not be possible without the support from NSERC Canada and Science Faculty of the University of Manitoba.

Thank you all for your impact on me and my research!

Chapter 1

Introduction

1.1 Mass Spectrometry of Biomolecules

A mass spectrometer (MS) is an analytical instrument that allows measurement of a molecule's mass-to-charge ratio, m/z . The types of mass spectrometers are various, from large and expensive electric and magnetic field sectors looking at isotopic patterns of exotic gases, to small and cheap quadrupole mass filters for detection in gas or liquid chromatography. Each instrument requires an ionization source to produce ions that can be manipulated with electric and magnetic fields. Ions are then separated based on their m/z ratio. Once the separation occurs, the ions are detected. The detector provides either spatial or temporal information that can be used to determine the ion's m/z value.

Although the principles of each instrument vary, they all need to have good accuracy and resolution. Accuracy is the ability to assign a proper m/z value to a detected peak. The resolution, $\Delta m/m$, is an ability to resolve two peaks that are close to each other. The resolution depends on the separation features of the instrument. The accuracy depends on the resolution, as well as proper calibration of the instrument.

Ionization techniques. Early mass spectrometers were limited by a small range of m/z ions. Ionization techniques produced heavy fragmentation of the sample. *Electron ionization (EI)* is one such technique [1]. An ion source filled with a gaseous sample is bombarded with electrons directly. Electrons knock out an outer shell electron, resulting in the ionization of a neutral analyte. Mostly gases, or specially modified small organic molecules can be processed effectively with this method. The energy imparted is ~ 70 eV. To protect an analyte from fragmentation, a buffer gas was introduced and the technique was called *chemical ionization (CI)*. Electrons bombard the buffer gas, ionizing it. Buffer ions then transfer their charge to the analyte via secondary reactions, such as proton transfer, charge exchange, cluster formation. Chemical ionization imparts less energy to the analyte, helping to reduce fragmentation of larger molecules.

Field ionization (FI) is one of the first techniques to produce ions directly from a solid. It opened the way to ionize non-volatile samples, up to 1 kDa. A heating filament is coated with the analyte and a high potential is applied inducing a proton transfer directly to the analyte [2]. With a help of the heating filament the analyte evaporates in vacuum.

Around the same time *laser ionization (LI)* was invented which also produces ions from a solid. It allows simple analytes to be ionized if the energy of the laser wavelength matches their ionization potential [3]. Simple organic molecules, such as phenothiazine and decacyclene, require no more than 5 eV of imparted energy to get ionized, making this ionization technique softer than electron ionization [4]. For larger molecules, however, a multi photon ionization is necessary. As the molecules de-excite, they release photons that can break chemical bonds holding an analyte together, leading to fragmentation. Working range of laser ionization is around 1 kDa [5].

Plasma desorption (PDMS) ionization is another method to produce ions from a solid. It involves the use of radioactive particles in MeV range, such as fission

fragments from decay of ^{252}Cf , to induce ionization and desorption of the analyte [6]. ^{252}Cf undergoes a spontaneous fission, resulting in two products flying in opposite direction. The method is well suited for time-of-flight mass spectrometry (TOF MS). TOF MS measures the time it takes for an ion to fly through a certain distance before hitting a detector. One product of fission bombards a target with analyte, volatilizing and ionizing it. The other product serves as a starting signal for a digital clock in TOF MS. Organic molecules up to 66 kDa can be seen with this ionization technique, although the practical range is less than 20 kDa. The ion source for PDMS produces around 3000 events per second into the solid angle of a target, and has a half-life 2.6 years. PDMS has been largely abandoned for other techniques with higher sensitivities and data acquisition rates. Newer techniques, such as fast-atom bombardment and secondary ionization, offer control over the intensity of produced ions and relative ease of use compared to PDMS.

Secondary ionization mass spectrometry (SIMS) has similar characteristics to PDMS. The technique involves a bombardment of solid analyte with primary ions in keV range. Analyte is imparted energy for both ionization and ablation. However, the method has a limited use with higher mass biomolecules due to damage it causes to the analyte. It also modifies subsequent layers. SIMS is routinely used for study of organic and inorganic solid samples up to 5 kDa. A special application of SIMS is in imaging mass spectrometry. It offers a sub-micron lateral resolution and variable intensity current.

By embedding an analyte in glycerol, and bombarding it with neutral atoms in keV range, it is possible to produce high intensity ions [7]. The technique is called *fast atom bombardment ionization (FAB)*. Unlike SIMS, FAB is resistant to damage. Glycerol is a liquid that provides regeneration of bombarded surface and provides high ablation rates. Mass range is similar to PDMS and SIMS. Sector instruments take advantage of high ion currents FAB generates.

Two recent techniques, *electrospray ionization (ESI)* and *matrix-assisted laser*

desorption/ionization (MALDI), became a revolution that gave an order of magnitude in mass range and 2–3 orders of magnitude in sensitivity compared to SIMS, PDMS and FAB. The invention of these techniques led to The Nobel Prize in Chemistry in 2002 [8]. ESI involves the spraying of analyte into a high electric field. Sample separates due to repelling Coulomb forces. Volatilization is enhanced by heating or vibration. Multiple charges are added to an analyte, lowering m/z -value even for large biomolecules. Electrospray is widely used with quadrupoles and traps, and conveniently coupled to HPLC. MALDI is a pulsed laser technique well suited for TOF MS. Sample is embedded inside an organic matrix. Laser ablates sample and ionizes it via various secondary ionization mechanisms. MALDI is well suited for time of flight mass spectrometers.

Types of mass spectrometer. A linear (or axial) time-of-flight (TOF) mass analyser is a very simple instrument. It provides unlimited mass range, parallel ion detection, high sensitivity and fast response. The first version of the instrument appeared as early as 1948, but had limited application because of its low resolution [9]. Coupled with the recent developments of fast digital electronics and soft ionization techniques that produce ions on a surface, it became a popular choice for biomolecule analysis [10]. The technique is essential for PDMS and performs well with pulsed SIMS.

In a simple linear TOF mass spectrometer the ions can be formed on the same plane, or within a small volume. Ions are injected linearly into the time-of-flight tube at the same time. The accelerating potentials are typically up to 20 kV. The ions gain the same kinetic energy. The ion velocity depends on the square-root of its mass, $v \propto \sqrt{m/z}$. This means that low m/z ions travel faster than high m/z ions. The ions drift in a linear fashion inside the flight tube where they are allowed to separate based on their m/z value. The linear flight tubes are usually 0.5–2 m long. A pulsed technique is necessary to produce a start signal when ions enter the time-of-flight tube, and a detector hit serves as a stop signal for the stopwatch. The pulsed

requirements make LI, MALDI and PDMS techniques well-suited for linear TOF MS. The frequency of ion production, however, should be low enough to prevent an overlap of information.

In the early days, the resolution in TOF MS was limited by the energy spread of ions produced in the source. Wiley and McLaren introduced both space and velocity focusing using a two-stage acceleration with their electron impact source [11].

They showed first that with suitable acceleration fields, ions with a pure spatial spread in the acceleration region are subject to space focusing, such that ions of the same mass but different initial location will reach the detector plane at the same time. This is because ions initially close to the grid acquire less energy in the acceleration region than more distant ions and therefore are overtaken by the latter after travelling some distance determined by their original position and the accelerating electric fields.

Secondly, they introduced *time-lag focusing* to correct for a pure velocity spread. In this technique, now usually called delayed extraction, a delay is introduced between ion production and the application of the accelerating fields, during which the ions drift freely. When the accelerating field is applied, the ions will be separated in space according to their velocity, allowing the same spatial bunching mentioned above to produce focusing.

In the general case described in detail by Wiley and McLaren, there may be both spatial and velocity spreads in the initial ion distribution, so some compromise is necessary to give optimum focusing. However, the two currently popular ionization methods, ESI and MALDI, approximate the two limiting cases described above. Ions suitably injected from an ESI source have an appreciable spatial spread, but a very small velocity spread (see below). A pure velocity spread is approximated by the geometry normally used for MALDI, since MALDI ions are ejected from an equipotential target by a very short laser pulse. In a simple linear TOF spectrometer, resolution can be optimized in both cases by using a two-stage acceleration region and setting the accelerating fields so that the focal plane coincides with the plane of

the detector.

In 1971, Mamyrin introduced an electrostatic mirror that reverses the direction of the ion flight [12], in order to compensate for small energy differences in similar m/z ions. Faster ions have a deeper penetration of the mirror, but spend less time in free flight, and with a suitable field, the ions are focused on the same plane when they reach the detector. A single-stage mirror consists of a single linear deceleration field and provides a first-order correction to the ion velocity spread [13]. A two-stage electric mirror, with independent electric fields, allows for a second-order energy correction [14].

The best performance of TOF instruments is now achieved by a combination of an electrostatic reflector and the Wiley-McLaren focusing techniques, and this combination is the basis for most current high-performance TOF systems. By themselves, the Wiley-McLaren focusing methods are limited because the narrowest time distributions are achieved for short flight paths, but good mass resolution requires long flight paths to provide time dispersion between ions of different mass. The electrostatic mirror provides energy focusing but does not compensate for time spreads in the source region, so by itself it also offers limited improvement. However, the two methods are highly effective when used in combination. The ions from the source are focused into a flat ion packet near the source and coincident with the object plane of the mirror. The mirror then images the ion packet onto the detector, greatly increasing the flight-time and therefore the time dispersion between species, without appreciably increasing the time spread.

There are several cases in which mass analysis of ions produced in a continuous beam (such as ESI) can benefit from the high efficiency and high mass range of TOF instruments. Orthogonal injection was introduced for this purpose in the early 1960s [15], but was rediscovered recently for applications with soft-ionization methods [16, 17]. In this method, a continuous beam of ions enters the TOF instrument perpendicular to its axis with low velocity and is injected into the flight path by a

pulsed extraction field directed along the TOF axis. Depending on the geometry, duty cycles of about 20% are typical in reflecting instruments, with the remaining 80% of the ions lost while injected ions drift to the detector. The advantage of parallel detection compared to scanning is much more significant.

Limits on the injection efficiency and the resolution are set by the spatial and velocity spreads of the injected ions. The properties of these instruments are therefore considerably improved if they are preceded by an ion guide running at relatively high pressure (up to ~ 10 Pa) to provide collisional cooling of the ions before they enter the TOF spectrometer [18]. In this way, a beam produced with a small energy spread, limited by thermal velocities, allowing effective spatial focusing as described above.

Orthogonal injection of MALDI ions was introduced to take advantage of the decoupling of the ion source from the mass spectrometer [19]. This largely removed the dependence of the instrument performance on the properties of the laser and the sample. The pulsed MALDI source is converted into a quasi-continuous beam in the collisional ion guide, and then injected at a high repetition rate, allowing more ions to be analyzed without saturating the detector. In this case, the 20% duty cycle is a disadvantage compared to an axial-injection system with effectively 100% efficiency.

Quadrupole mass spectrometer (QMS) is another type of mass analyser. It was first developed by Wolfgang Paul [20]. The instrument separates ions with different masses using a quadrupole electrical field with a superimposed radio-frequency field, established by four parallel rods at the corners of a square. He received The Noble Prize in Physics, 1989, *for the development of the ion trap technique* [21]. The motion of the ions depends on their m/z value [22], such that only ions of a narrow m/z range have a stable trajectory. Due to this selectivity, quadrupole fields act as mass filters. QMS m/z range is typically 2000 and the accuracy is hundreds of ppm. Its resolution is limited by the time an ion spends inside the quadrupole field. QMS sensitivity decreases when the resolution increases, leading to poorer signal from the heavier ions. QMS is well suited for gas and liquid chromatography coupled to electrospray

interface due to its ability to process large volume of ions. The ions produced by ESI are in general no more than $m/z = 2000$, due multiple charges added to an analyte.

The same rod configuration used for QMS can act as an ion guide that operates only in RF-only mode allowing all the ions to pass through unhindered. The initial ion kinetic energies do not need to be consistent, because the quadrupole field overrides them easily. Linear guides are used in collision-induced dissociation cells (CID), where complex ions are collided with a neutral inert gas to induce controlled fragmentation [23]. The use of CID cells is very important for *de novo* sequencing of unknown peptides.

Quadrupole instruments are easily coupled in tandem with other instruments. For example, triple quadrupole instrument (QqQ) [24]. It combines three quadrupoles sequentially. First and third quadrupole sections act as a mass filter (Q), and second quadrupole section acts as a collision-induced dissociation cell (q). An ion is selected for the fragmentation in the first quadrupole. The fragmentation occurs in the second quadrupole. Each fragment is analysed by scanning the third quadrupole. Overall QqQ has a low sensitivity due to scanning nature of the last quadrupole. Once daughter ions are generated in CID cell, only ions in a narrow m/z -range can be detected. Hybridization with other mass analysers is necessary to improve instrument's sensitivity.

A need to acquire a simple mass spectrum (MS), as well as the collision-induced fragmentation spectrum (MS/MS) pushed combining quadrupole fields with the time-of-flight mass spectrometers. TOF machines are fast and offer a parallel detection, and CID cells provide the necessary fragmentation for the peptide identification. A first such machine had a single CID cell coupled to a linear time of flight tube [25]. The instrument interfaced with a thermal desorption probe. It allowed to perform fragmentation with daughter ions analysed right after in a TOF MS.

The first coupling of cooling quadrupole cell with orthogonal injection time of flight was done by research group at the University of Manitoba [18]. The initial kinetic and

thermal energies of the ions coming out of the ion source are gently transferred to the cooling gas by means of a two dimensional oscillation and collision [26]. The collisional energy with inert gas is below 10 eV to prevent fragmentation. This makes an energy spread in the axis of the injection very small and tolerable, and improves resolution and sensitivity of the instrument. The ions leaving the quadrupole segments tend to spread along the quadrupole axis, turning pulsed beam of ions into a quasi-continuous beam. As a result, combining collisional cooling and orthogonal injection TOF MS reduced dependence of peak broadening on the energy spread inside the ion source. ESI and MALDI ionization techniques are routinely used on the same instrument without a need to change much of the settings. The same principles apply to an addition of a CID cell. As the method evolved, both MALDI and ESI ion sources are now coupled to tandem mass spectrometers. Nowadays, such instruments come with 40,000 (FWHM) resolution, low ppm accuracy, low attomole sensitivity and the ease of use. Due to a large ion capacity and parallel detection of TOF analysers, the instrument's early applications were on-line liquid chromatography coupled to MS/MS analysis.

1.2 Matrix-assisted laser desorption/ionization

Matrix-assisted laser desorption/ionization (MALDI) is a powerful technique that allows conversion of complex organic compounds, such as peptides, sugars and lipids, from a solid to a gas phase, while ionizing them. The discovery of the technique led to part of The Noble Prize in Chemistry, 2002, shared by John B. Fenn and Koichi Tanaka *for their development of soft desorption ionisation methods for mass spectrometric analyses of biological macromolecules* [8]. Fenn developed the electrospray ionization technique [27, 28], and Tanaka developed a variant of conventional MALDI. Tanaka mixed protein sample with glycerol containing cobalt particles, and used a nitrogen laser to induce ablation and ionization of the analyte [29]. The laser

of 337 nm wavelength was not absorbed by the protein, but by the cobalt particles instead, preventing fragmentation. Ionization was presumed to happen via additional reactions once both matrix and the analytes were in the gas phase, adding a positive charge to an intact protein.

An earlier, and ultimately more successful variant of this techniques was introduced by Karas and Hillenkamp [30], although the high mass capability was not demonstrated until 1988, after Tanaka's revelation [31]. Initially they used nicotinic acid as the matrix to absorb the wavelength of the radiation. The organic matrix introduces a buffer and protects the analyte from the laser energy. It is responsible for desorption and ionization of the analyte. Three more matrices were discovered shortly after that are now widely used in various applications: 3,5-dimethoxy-4-hydroxycinnamic acid [32], 2,5-dihydroxybenzoic acid [33] and α -cyano-4-hydroxycinnamic acid [34]. The further developments of MALDI revolved around finding new and more efficient matrices, understanding of fundamental principles and finding practical uses and applications for the analysis of the organic macromolecules.

The role of the laser parameters and the energy transfer is important in the MALDI process. An organic matrix needs to absorb at least the amount of energy equal to its heat of fusion and vaporization to undergo a phase change. For safe phase transition the analyte must be integrated into and completely surrounded by the matrix lattice structure. The analyte to matrix ratio varies between 1:1,000–50,000 molar ratio. The efficiency of the MALDI process depends on the photon wavelength and the absorption of the matrix for that wavelength [35]. If the matrix absorption lies on the edge of the laser's wavelength, then the ion yield suffers. The quality of the formed plume depends on the length of the pulse. For ultra-short laser pulses in the range of a few femtoseconds, the photo-dissociation by non-linear processes occurs. In this case the pulse is shorter than the average time for matrix ionization and if one or more photon energies match the bonding energy between atoms comprising the analyte molecule, fragmentation can occur [36]. The longer pulses (~ 25 ns) lead to

the analyte degradation via the destructive thermal excitation [37]. A typical laser pulse used in MALDI is 0.5–10 ns. Laser pulses on the shorter range result in the better quality plumes due to higher plume pressure build up [38]. Plumes with higher initial pressures produce less analyte-matrix clusters.

The mode of ablation of neutral compounds depends on the fluence of the laser. Johnson suggests that for low fluence each laser pulse removes matrix layer by layer until all of the matrix in a given spot is consumed [39]. A smooth transition from solid to gas phase takes place via desorption of matrix molecules. As the laser fluence increases, the scale of the phase change rapidly increases. At high laser fluence the system absorbs more energy than a combined energy of melting, sublimation and other types of phase transitions. Eventually, the system goes into a superheated state prior to going into a gas phase, and large matrix chunks are ejected into gas phase [40]. In any mode, the result of matrix desorption is a plume of gas rapidly expanding into the vacuum.

A number of models try to predict the behaviour of the gaseous plume. The axial component of plume geometry is reported to be larger than its radial component, resulting in a uni-modular distribution of gas [41]. The plume dynamics seem to be independent of initial conditions. The ion internal energies are predicted by the matrix sublimation temperature [42] and the nature of fragmentation is tied to the proton affinities of the matrix [43]. Some simulations and models suggest that the gas plume undergoes an expansion, leading to a cooling off effect, where the matrix and the analyte undergo a reduction in internal energies [38, 44]. A number of reactions happening inside the plume decreases, and the gas pressure reduces. If the initial plume pressure is low, as in the case of long laser pulses, some analyte-matrix clusters may be formed. Shorter laser pulses can decrease the amount of clusters. The simulations predict that for all pulse widths about two thirds of the material is ejected as separate molecules [38].

Two theories of ionization emerged recently. One model predicts that the cluster-

analyte interactions are responsible for an ionization. They are ejected from a target surface during desorption step of MALDI, and can be easily detected by increasing an ion source operating pressure [45]. Clusters consist of matrix-matrix, matrix-analyte, matrix-water, and other charged complexes, and are held by hydrogen bonding and Coulomb interactions [46]. Clusters are ejected either neutral due to the overall balance of ions and counter-ions, or with a charge induced by disruption of analyte-matrix lattice during the desorption step. Many analyte molecules come pre-ionized with the help of ion pairing reagents, such as trifluoroacetic or a formic acid. Ion pairing reagents lower pH of the solution, stabilizing the charge on peptides. During crystallization, the charges get trapped inside the matrix lattice. Once in the gas phase, a number of charge-reducing mechanisms take place. These include neutralization of analyte by counter-ions during cluster dissociation, generation of new neutral clusters, absorption of photoelectrons and free metallic electrons [47]. When an analyte ion dissociates from a cluster and avoids charge-reducing reactions, it can be detected as a protonated species by a mass spectrometer. Species of sufficiently high m/z value have a greater chance of maintaining higher charge states than smaller species.

The other model involves fluorescence theory [48]. Knochenmuss *et al.* break down the ionization into primary and secondary reactions. Primary reactions ionize matrix, and secondary reactions ionize analyte. According to this model, a matrix molecule gets excited to its first excited state by the laser. If another excited matrix molecule is located within 20 molecules, its de-excitation energy can be pulled to excite a first matrix molecule to an even higher energy state [38]. In this way, it is possible to ionize one molecule of matrix. The model suggests that the energy pooling is the primary ionization mechanism in MALDI. An experiment conducted by Jaskolla *et al.* seems to support parts of this claim. A temperature-sensitive molecule, such as N-p-methoxybenzylpyridinium ion, undergoes dissociation at a certain temperature [49]. By varying the temperature, it is possible to turn the dye into a fluorescent

trap. The group showed that by activating the molecule it completely shuts down the MALDI process by trapping laser energy. The trapped energy decays as vibrational energy.

Secondary reactions are responsible for analyte ionization and may include proton transfer, alkaline cationization and neutralization of free radicals. Some ionization theories suggest that plume reactions are driven by proton affinities of the species involved [50]. Species with greater basicity are more likely to receive positive charge from proton transfers. Although there are many simulations that try to explain the production of mostly +1 species [51], there is no experimental evidence to support them.

More recent theories try to combine together fluorescence and analyte-cluster interactions. They suggest that MALDI ionization is comprised of two independent mechanisms. This independence can be targeted to boost one ionization mechanism over the other. For example, Karas *et al.* suggest to decrease pH of the solution before the sample is mixed with the matrix to improve the survival chances of charge in clusters [52]. On the other hand, Knochenmuss *et al.* propose to use higher laser fluence to increase the rate of energy pooling, which should have little effect on pre-formed charges in clusters [53]. Matrices with high proton affinities are predicted to inhibit secondary reactions in fluorescence model, but help to maintain charge in clusters.

Combined theories are able to explain the matrix suppression effect, when at low fluence and high analyte concentration a lack of charged matrix molecules is observed. However, it can only partially explain the analyte suppression, when a particular analyte signal is lacking due to presence of other sample species in the sample. Experimental work still needs to present concrete evidence to support the validity of the above models of MALDI ionization.

1.3 Imaging Mass Spectrometry

One of the applications of mass spectrometry is mass-selected imaging of biological tissues. A two-dimensional image carrying mass spectroscopic information can be extracted from a tissue. The pixel size is defined by lateral resolution of the ionization method in place. Imaging mass spectrometry (IMS) has an advantage over other imaging techniques, as its mass selection provides chemical identity. Peptide sequences, and chemical or biological modifications can be identified. IMS allows monitoring of expression of biological products in different diseases and conditions, as well as to recognize a malignant from a normal tissue [54]. The imaging can track the locations of where the drugs are deposited, as well as the metabolite expression.

Common ionization techniques used in the imaging mass spectrometry of tissues are matrix-assisted laser desorption/ionization (MALDI), secondary-ionization mass spectrometry (SIMS) and several new atmospheric ionization methods such as desorption electrospray ionization (DESI). DESI is an atmospheric ionization technique that employs the electrospray as a primary mechanism for ionization and desorption of the sample directly from a tissue. Charged droplets are delivered to the surface of a tissue with a small capillary. Droplets dissolve and ionize the sample, and evaporate via the usual electrospray mechanism. Charged sample is then analyzed with a mass spectrometer [55]. DESI is convenient to use due to it being an ambient ionization technique that requires no matrix. The lateral resolution depends on the distance between a capillary and a tissue, nebulization gas pressure, solvent flow rate and solvent composition. A 250 μm lateral resolution is routinely achieved, which is inferior to other imaging techniques.

SIMS uses primary metal ions to bombard a surface of the tissue, leading to creation of secondary ions that are then collected and detected [56, 57]. SIMS can produce very small beams, less than a micrometer and does not require the use of the matrix. SIMS is usually used for smaller molecule analysis. SIMS can perform depth profile, removing sample layer by layer. It is used in the industry for testing inorganic

materials. Unfortunately, the primary ions permanently modify the subsequent layers of the analyte, making repeated acquisition of the spectra from the same spot yield different results. SIMS is much less sensitive overall, limiting its use for proteins. However, secondary ionization gives best spatial resolution for lipid analysis.

MALDI, on the other hand, provides a high mass range and high sensitivity but with routine lateral resolution typically $\sim 100 \mu\text{m}$. However, competing processes, such as analyte suppression effect, can interfere with detection of small m/z -value drugs. An addition of wet matrix introduces a protein migration. In order for MALDI to function properly, some integration of the analyte into the matrix lattice is necessary. Commonly used spotting technique displaces analytes from their original location. This introduces inaccuracies in spatial information. Proteins suffer more from this displacement than lipids.

The following matrices are often used with MALDI imaging mass spectrometry. Sinapinic acid (SA) is used for protein profiling [58]. SA however is not suited for small peptide analysis, as it produces poor spectra for ions below 2.5 kDa. α -Cyano-4-hydroxycinnamic acid is used for small peptide analysis instead. The spotting of these two matrices produces small crystals, which is an advantage over other matrices, such as 2,5-dihydroxybenzoic acid. Protein lateral resolution is limited to $\sim 100 \mu\text{m}$ and lipid resolution is 10–50 μm . An interest in the MALDI IMS development has increased lately as a replacement for SIMS.

A biological tissue contains a variety of proteins, peptides, sugars and other biological molecules, and sensitive detection of these molecules is a critical figure-of-merit for imaging. One of the ways to improve sensitivity is to use small beam spots (see below). Although the spatial resolution is ultimately limited by the sample preparation techniques, optical efforts, such as the microprobe [59] and the near-field objective [60], allow the use of sub-micron laser beams. An understanding of fundamental relationships between laser fluence, spot size, ion yield per shot and sensitivity is necessary to improve the dynamic range of MALDI imaging.

1.4 Sensitivity in MALDI

In most investigations of MALDI performance, the ion yield, defined as the ion per laser shot, is studied. However, the question of sensitivity is essential for MALDI imaging. It determines the number of ions produced from a given area of tissue and therefore limits spatial resolution for particular analysis.

The sensitivity in MALDI depends on various factors. Matching a laser wavelength to matrix optical absorption peak is necessary. The understanding of laser parameters is important for the optimization of the ablation process, as well as the ion yield and the sensitivity. Laser pulse width affects plume dynamics as discussed earlier. The energy area density, also known as the laser fluence, influences ion yield and the sensitivity. Laser fluence dictates whether the ions are detected or fragmented. A large area of irradiation increases the ion yield per shot, but does so at decreased efficiency. Homogeneous, Gaussian or speckled beam profiles have different effects on the sensitivity and ion yield. The choice of the matrix and the matrix-analyte ratio determines whether the matrix competes with or promotes analyte ionization. Understanding fundamental processes can hint what parameters to target for the optimization. Developing experimental practices, as well as theoretical models is necessary to further improve the sensitivity of the MALDI process.

Two common laser types are used for MALDI, nitrogen gas discharge laser (337 nm) and Nd: YAG laser (355 nm). Both lasers roughly target the optical absorption peak of the α -cyano-4-hydroxycinnamic acid (CHCA) [61, 62]. Nd: YAG laser tends to have a lower energy output than the nitrogen laser, but it has a faster repetition rate to compensate for the lower ion yield. The shape of the laser beam profile plays a bigger role on ion yield than a slight mismatch of the wavelengths with the matrix absorption peak. Both nitrogen and Nd: YAG lasers produce a speckle pattern, with many local peaks due to laser mixing modes [63]. Nd: YAG produces sharper spots, with a rapid laser intensity drop off outside of the local maxima, whereas nitrogen beam shows a slower drop-off effect. A nitrogen laser has the best ion yield per shot.

The modulation of optic fibre can increase the ion yield of Nd: YAG laser [62, 63]. A version of speckle beam is being promoted by Bruker Daltonics, called *smartbeam* [62]. The pattern is produced by a proprietary modulator. They reported higher ion yields from smartbeam than from a regular Nd: YAG laser. However, there is a simpler way to improve the sensitivity of Nd: YAG laser. By continuously twisting optic fibre, one can mix laser modes and produce a more homogeneous laser profile, increasing irradiation area [63].

The effects of laser fluence were studied at the energies below the threshold and above the saturation levels. The fluence (F) is directly proportional to the laser energy (E), and inversely proportional to the area of laser spot (A), $F = E/A$. Early belief was that there is a laser fluence threshold below which no ions are produced [64, 65]. Westmacott *et al.* showed that MALDI does not involve a hard threshold fluence, but a step dependence of the ion yield on fluence appears in practice like a threshold [66]. Typically, the threshold fluence is taken to be the fluence at which a single laser shot produces an ion signal-to-noise ratio greater than 2 or 3. As such, it clearly depends on the geometry and transmission efficiency of the instrument. When the laser operates at fluences below a threshold value, a Poisson distribution governs the ion detection. A threshold therefore is a technical limitation of hardware rather than a fundamental feature of MALDI. Above an ion threshold the ion yield rapidly increases with an increased fluence following a steep power-law, until a saturation point is achieved. Saturation point is reached when the ion yield cannot be improved by increasing fluence. At saturation levels and above the yield decreases slowly due to various fragmentation mechanisms.

Laser spot size has an influence over the amount of ions produced in MALDI. An ability to focus laser beam to smaller area results in an increase of fluence. Below saturation, ion yield per shot shows a cubic dependence on the area [65, 63], leading to overall less ions for smaller spots. At saturation levels there is a linear dependence between the ion yield and the fluence. However, decreasing the spot size, as well as

increasing the fluence was shown to increase the sensitivity [63]. Qiao *et al.* showed that higher saturation levels can be achieved by using smaller laser spots. If enough fluence is channelled to a smaller spot, total ion yield deficiency can be compensated by an increased sensitivity from a smaller area of irradiation. A number of spot sizes were tested, from 200 μm to 10 μm in size. A power law also governs the sensitivity with respect to fluence. The results extend to 3,5-dimethoxy-4-hydroxycinnamic acid, 2,5-dihydroxybenzoic acid, α -cyano-4-hydroxycinnamic acid and potentially to other matrices. The results stay consistent for peptides and proteins in 1–24 kDa range. Guenther *et al.* conducted a similar study with an atmospheric pressure (AP) MALDI source [67]. They used lower fluences to reach an apparent threshold, and were able to reach higher saturation levels than previously reported. The results were attributed to a better transmission of their co-axial ion source, as well as an employ of atmospheric pressure [68]. Guenther used a Gaussian instead of a flat-top profile employed by Qiao. Gaussian beams have a spatial dependence on the energy channelled to the spot, leading to a slower response of ion yield per shot with respect to the fluence. Although there is no detailed study of ion yield response for larger than 10 μm spots for the atmospheric MALDI, Guenther was able to confirm that for laser spot sizes between 1 μm and 8 μm the sensitivity improves with smaller spot sizes. Higher levels of saturation can be achieved with smaller beam sizes.

Guenther *et al.* were able to profile sensitivity for sub 10 μm laser spots. However, a direct comparison to Qiao's work is not apt due to difference in operating pressures inside the ion source (atmospheric pressure versus vacuum). Different plume dynamics take place at different pressures as discussed earlier. Unfortunately, the sensitivity studies for AP MALDI for larger than 10 μm laser spots were not conducted at the time of this thesis. Making conclusions if the trends extend for larger spots are not possible without further research. Qiao *et al.* clearly showed that sensitivity increases with smaller laser spots down to 10 μm and higher fluences. The goal of this project is to see if laser spots below 10 μm offer any practical use. This can be achieved with

fibre or fibre-less geometries. Both geometries have advantages and disadvantages. Fibres provide flat-top beam profiles, whereas fibre-less configuration directly images Gaussian-like beam profile at the target surface. Gaussian-like spot sizes have a dependence on the channelled energy, whereas flat-top spots do not change their size with an increased energy per shot. Fibre-less configuration offers better laser transmission than small fibres, extending the range of available fluences.

Chapter 2

Experimental

2.1 Mass Spectrometry

For our experiments we have modified a component of a prototype of a commercial instrument from MDS Sciex, ProTOF [69]. It is an orthogonal-injection time-of-flight mass analyser, coupled to two quadrupole ion guides and a custom-built ion source with a normally incident laser well suited for our experiment. An overview of the instrument can be seen in Figure 2.1. By guiding the laser beam through an optical system to the sample, the ion source generates ions via the MALDI process. Ions are then guided through two quadrupole ion guides. The ion guides cool the MALDI plume and are used to steer the ions along the axis of their longitudinal symmetry. Both ion guides have the facility to accelerate the ions along the axis to minimize the time to injection. The original purpose of the instrument was to support ion mobility experiments, so two quadrupole ion guides were installed. For this experiment they are used to simply guide ions to the mass analyser. The first ion guide is a segmented quadrupole set. It consists of smaller sections connected by resistors. Ions entering this ion guide experience a linear acceleration, as well as cooling with an inert gas. The second ion guide is a normal quadrupole section augmented with tapered metal strips under a constant DC voltage [70]. As ions move through this ion guide, they

experience a small axial field along the lateral axis. By varying DC voltage, it is possible to speed up or to slow down the ions. Deflection plates are used to steer the ions into a modulator section of the time-of-flight mass analyser where they are injected into the analyser orthogonally to the quadrupole axis. Ions then drift in the field-free region to separate based on their m/z value. A two-stage electrostatic mirror is used to compensate for the energy spread and to focus ions onto the plane of micro-channel detector. The detector registers the ion arrival and sends a signal to the electronics to convert the measured time-of-flight into a useful m/z information. The results are recorded on a computer using a software developed in-house. Our instrument has a mass resolution of about 10,000 (FWHM) in the mass range of substance P (1347.6 Da), and a mass accuracy around 10 ppm. In this section I will outline the reasoning and the purpose behind the use of this particular instrument and its components.

2.1.1 Ion source

A UV-MALDI ion source for a mass spectrometer has a laser beam of appropriate wavelength and fluence range delivered to a sample embedded into an organic matrix. Often these ion sources are accompanied by either a simple or a complex system of optical components. The ion source also guides the generated ions into the mass spectrometer. For imaging purposes, the ion source also provides a means to raster the laser across the surface of our sample. The ion source consists of two parts: a flexible optical system located outside of the instrument, as well as the target-holding motors and the ion optics exposed to the instrument vacuum.

Optical systems

The laser can be introduced directly using mirrors and lenses (fibre-less mode) or it can be coupled to an optic fibre which is imaged at the plane of a target (fibre mode). Both modes have their advantages and disadvantages. The fibre-less mode

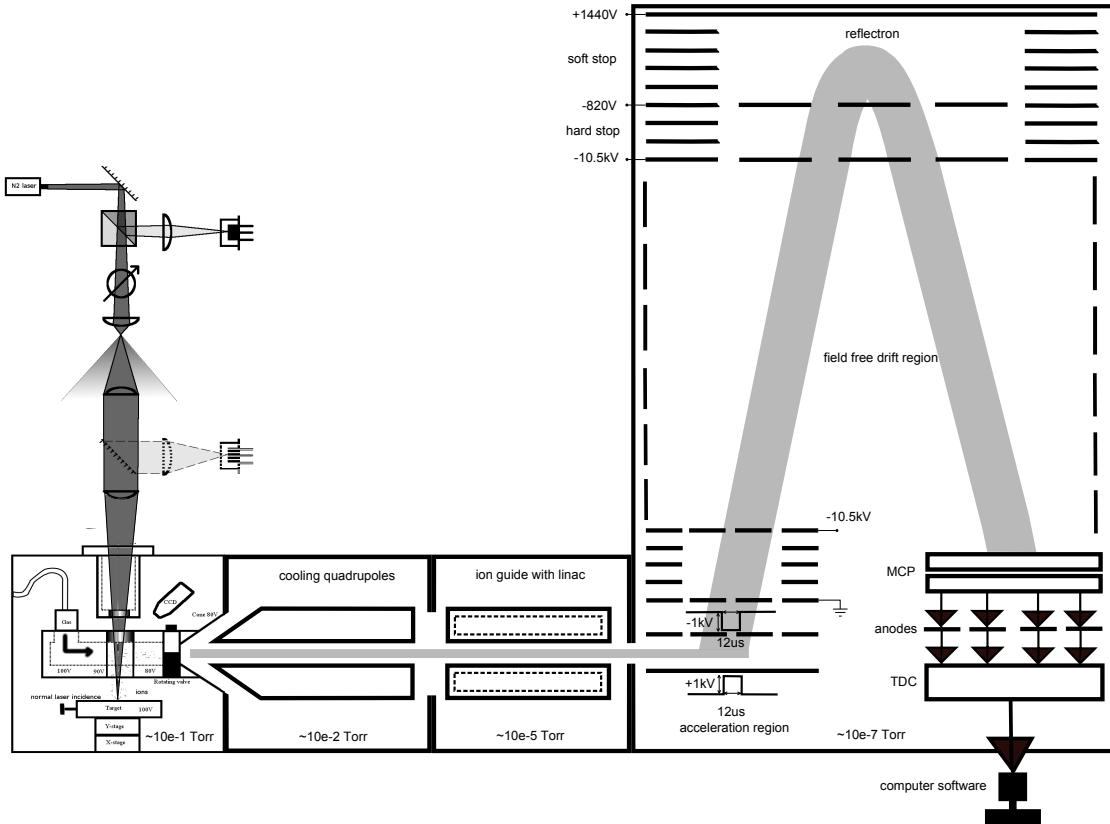


Figure 2.1: Orthogonal time-of-flight mass spectrometer with a custom quadrupole and an ion source sections. This particular arrangement is using a fibre-less optical system to deliver laser beam to the target.

can produce smaller spots, but produces a Gaussian profile which causes a dependence of the effective spot size on the laser fluence. The use of the fibre optic gives a top-hat energy profile with a well-defined spot size, but there is a limitation how small the spot can be within a useful laser fluence range. In our experiment, we have employed a flexible optical system that allows us to switch easily between the optic fibre and the fibre-less configurations (Figure 2.2). They have some common features, and some features that are unique to each set-up. The system uses a pulsed laser (Laser Science, Inc., VSL-337ND-S). Two $\frac{1}{8}\lambda$ precision elliptical flat mirrors (Edmund Optics, UV Enhanced Aluminum) are used for guiding the laser beam. Both set-ups employ one or two circular variable neutral density filters (Edmund Optics, 0.0–2.0 OD) depending on the fluence needs. We also used an optional insert for both set-ups to examine the

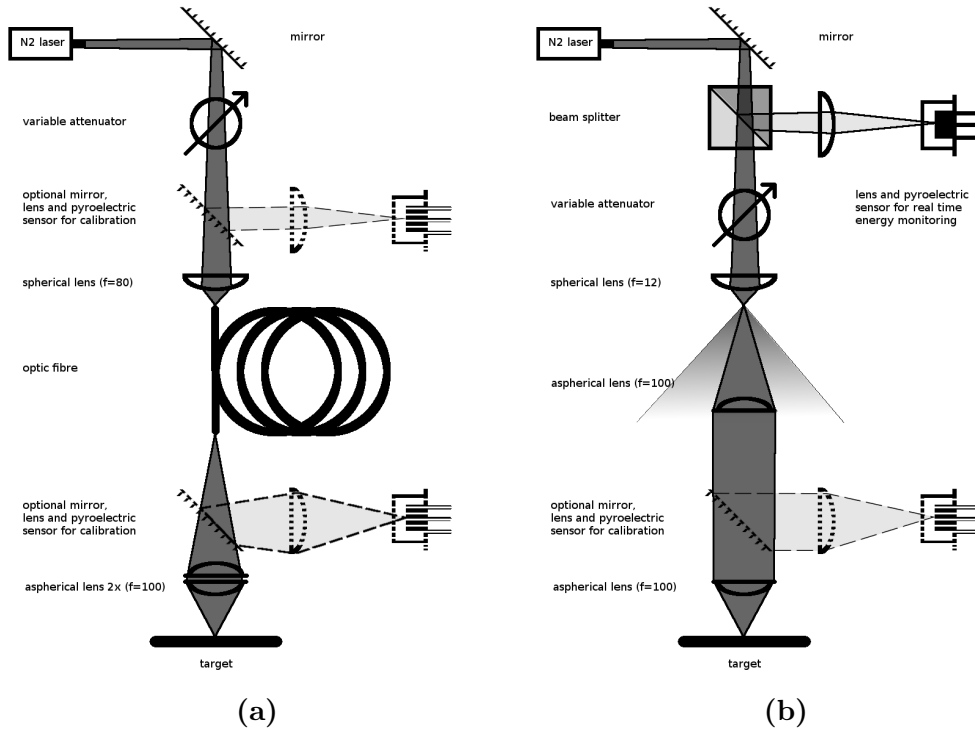


Figure 2.2: Two on-line optical configurations in use: a) an optic fibre is used to guide laser beam to the target, b) laser beam is directly coupled to the target.

beam profile. This insert can be placed anywhere on the vertical optical bench above the target. It consists of a precision flat mirror, a 80 mm plano-convex lens (Edmund Optics, UV Fused Silica) for focusing and expanding, a shrinking or a parallel laser beam on a surface of a pyroelectric sensor (Coherent, J3-05). The sensor is coupled directly to a digital oscilloscope (Tektronix, TDS 520). By measuring the height of a produced peak on the oscilloscope, it was possible to measure the energy levels of a laser beam at any given place, at any given time. All components were secured by posts and riders on a 1 m long vertical optical bench from Edmund Optics and Melles Griot.

Fibre Optics. For the fibre set-up (Figure 2.2a), we used an 80 mm focal length plano-convex lens to channel a laser beam to an optic fibre. A range of fibres has been used for the experiment: 10–200 μm diameter (OZ Optics). Fibres mix laser modes and produce relatively flat energy profile when the beam emerges [66, 63], Figure 2.3.

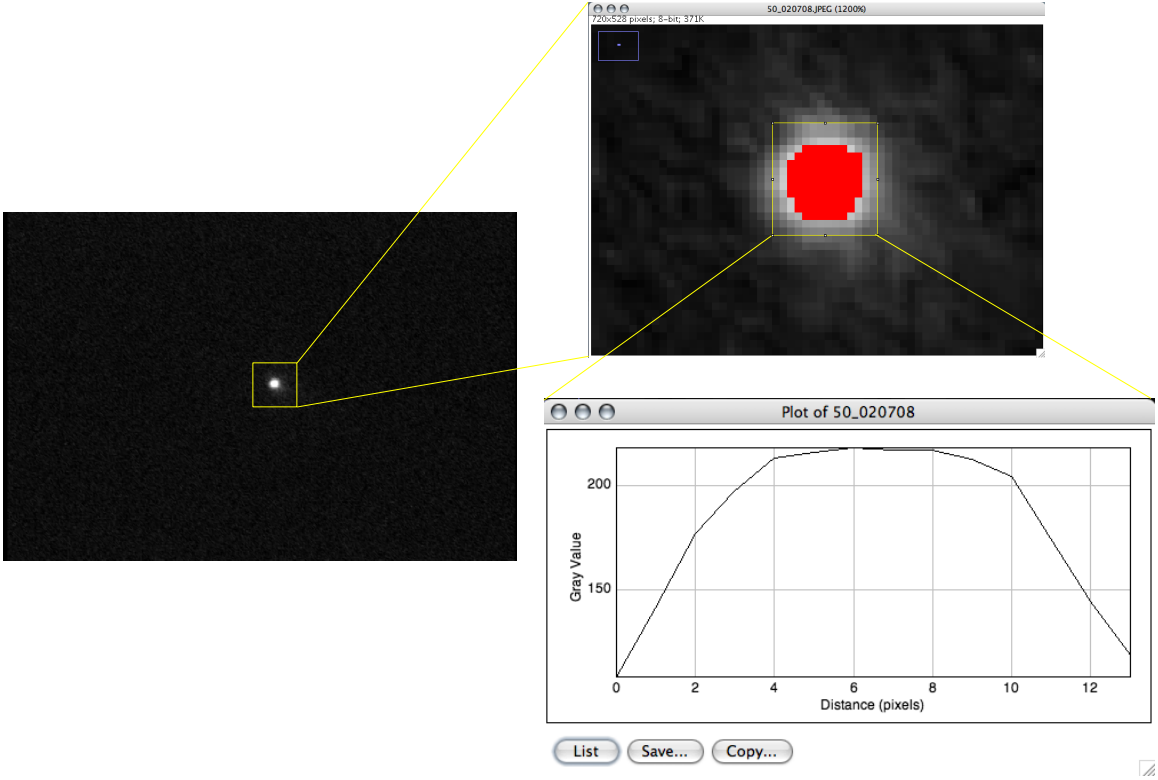


Figure 2.3: Energy profile of the fibre beam.

A fibre is then imaged by a pair of the aspherical lenses (R. Mathews Optical Works Inc., UV Fused Silica). The aspherical lenses can also be physically separated from each other, and moved around relative to the fibre and a target plane. It is necessary if we are to produce the smallest spot size. The use of aspherical lenses is critical as spherical lenses for this system would produce spherical aberrations on the order of 0.25–0.60 mm, depending on the magnification. The transverse magnification is governed by

$$M_T = \frac{1}{f^2}(s_i - f) \left(d - \frac{f s_i}{s_i - f} - f \right) \quad (2.1)$$

where s_i is the distance to the target from the last lens, d is a separation between two aspherical lenses, and f is the focal length of the lenses involved. The limiting factor in this case was how close we could install a final aspherical lens to the target, which was 7 cm. Taking into an account the physical constraints and a requirement that a target has to be in a vacuum, we were able to achieve a magnification $M_T = \frac{1}{2.4}$.

Fibre-less Optics. For the fibre-less set up, we coupled a laser beam directly to the target through a lens system shown in Figure 2.2b. The beam is diverted through either one or two neutral density filters for the fluence control. A short plano-convex PVX spherical lens (Edmund Optics, UV Fused Silica) was used to focus the laser beam to a small spot. The smallest theoretical beam size at the point of focus, ignoring spherical aberrations, is

$$D_w = f\theta \quad (2.2)$$

where D_w is the diameter of the beam waist, the narrowest point on the laser beam, f is the focal length of the focusing lens, and θ is the beam divergence. Since we are taking the laser beam directly out of the laser, the divergence angle is supplied by a manufacturer, 0.3×10^{-3} rad. A theoretical beam spot size after the short spherical lens is then

$$D_w = (12 \times 10^{-3} \text{ m})(0.3 \times 10^{-3}) = 3.6 \times 10^{-6} \text{ m} \quad (2.3)$$

After a laser beam has been reflected by a flat precision mirror, it is directed through a beam splitter and a set of a 80 mm plano-convex PVX lens and a pyroelectric sensor attached to a digital oscilloscope to monitor the laser's energy variation in real time. Around 11% of the beam's energy has been diverted for this purpose.

In order to reduce the spherical aberration effects on the final image, the short spherical lens ($f_1 = 12$ mm) defocused beam (Figure 2.4b). Part of this defocused beam has been collected by a plano-convex aspherical lens ($f_2 = 100$ mm). This way the radius of the aspherical lens acted as a diaphragm ($h_2 = 25$ mm), and the collected beam still carried enough energy for the MALDI process to occur. The separation between two aspherical lenses, d , as well as object and image distances, s_o and s_i respectively, will affect the transverse magnification of the imaged spot created by the spherical lens. The larger is s_o , the smaller amount of spherical aberrations are introduced into the system. The larger is s_o , the smaller amount of beam is collected, leading to smaller range of fluences in use. Figure 2.4a shows a fibre configuration

with 1-to-1 magnification, however, for a given s_i , s_o and d two configurations will give the same transverse magnification.

The fibre-less configuration employs a spherical lens, which limits the spot size of the laser beam due to spherical aberrations. It is impossible to focus a source point to another infinitesimally small point at the image plane [71]. The smallest possible size a source point can be focused to is known as a circle of least confusion. Its size can be estimated to be

$$CLC \approx 2 \left(\frac{R}{8} \Theta_r^3 + \frac{19R}{128} \Theta_r^5 \right) \quad (2.4)$$

where R is the radius of the lens curvature, and Θ_r is the largest refracted angle. In our configuration, the largest incidence angle can be shown to be $\Theta_i = \sin^{-1} \frac{h_1/2}{R_1} = 56.44^\circ$ (Figure 2.4b). Using the Snell's law, the largest refracted angle becomes $\Theta_r = 31.88^\circ$. Our spherical lens produces a $265 \mu\text{m}$ circle of least confusion for a perfect parallel beam. By introducing a diaphragm we essentially remove most of the rays responsible for broadening of circle of least confusion and reduce the effect of spherical aberrations. The circle of least confusion with a diaphragm becomes $2.3 \mu\text{m}$ and $0.4 \mu\text{m}$ for 1-to-1 and 2.4-to-1 configurations respectfully. Adding spherical aberrations and predicted spot size in quadrature leads to 4.3 and $3.6 \mu\text{m}$ respectively.

Both configurations suffer from energy loses. Depending on the magnification and an optic set-up in use, a certain amount of energy was cut off due to first aspherical lens acting as a diaphragm. For fibre-less optics (Figure 2.4b), assume the laser beam has a perfect Gaussian profile. The percentage of the laser power contained in a circle of radius ρ_0 is

$$P = \left(1 - \exp \left[- \frac{2\rho_0^2}{W^2(s)} \right] \right) \times 100\% \quad (2.5)$$

where $W(s)$ is a size of the beam at a longitudinal position s . Let the aspherical lens to be located at the position s_o , and to have a fixed diameter of 25 mm . The power

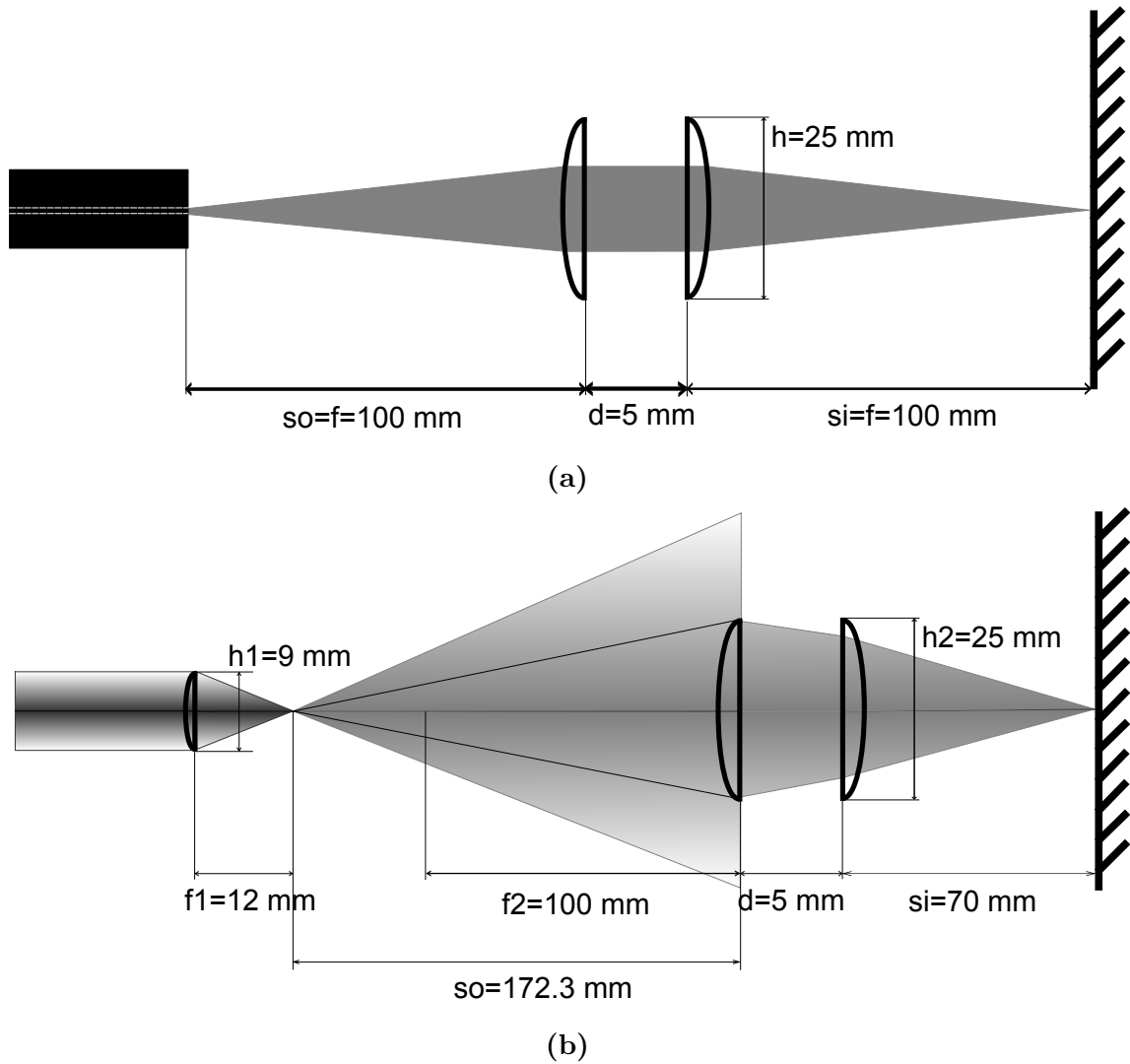


Figure 2.4: Two off-line optical configurations used for testing: a) an optic fibre is imaged in 1-to-1 configuration, b) beam is focused by a short spherical lens and then imaged in 2.4-to-1 configuration.

collected by the lens is

$$P = \left(1 - \exp \left[- \frac{2(0.25 \text{ m})^2}{W^2(s_o)} \right] \right) \times 100\% \quad (2.6)$$

with $W(s_o)$ defined by the magnification. For 1-to-1 magnification, the first aspherical lens tends to be located closer to the defocusing lens, and s_o value is larger in a 2.4-to-1 configuration (Figure 2.4b). For 1-to-1 configuration, more energy is collected, because $W(s_o)$ is smaller for shorter s_o values. Roughly 7.8% and 2.7% of total laser power has been collected for 1-to-1 and 2.4-to-1 configurations respectfully, making the system relatively inefficient. For the fibre set up, we had to manually check if the beam was larger than the window of entry. If the beam was large, the energy losses were estimated based on a geometry argument. The limiting factor there was a numerical aperture of the optic fibre in use. The energy losses in the fibre configurations are fixed for a given geometry. For more intense energies however, the fibre degraded due to heating issues, and the transmission decreased. It was necessary to measure the fibre energy output before and after the experiment to make sure that the damage was not done.

The effective spot size of the beam is assumed to be the size of the burn mark produced during the MALDI process (Figure 2.5a). It usually differs from the optical spot size due to various physical phenomena taking place at the matrix surface during the laser beam exposure. For a given optical set-up the effective spot size of a laser beam largely depends on the amount of delivered energy. The effect of laser energy on a spot size is more profound for smaller spot sizes. Prolonged exposure to the larger fluences of the beam damage the tip of the fibre and ultimately change its transmission as well. The effect of laser energy on a spot size for the fibre-less optics would be even more profound, because of Gaussian shape of the beam. Therefore it is necessary to measure the energy of a laser beam at any given time, before, after and during the experiment. This was achieved by the use of the optional insert

depicted in Figure 2.2. A fibre-less set-up required constant monitoring. We used a permanent beam splitter coupled to a plano-convex lens and a pyroelectric sensor for an on-line energy monitoring. A separate insert before the beam entered the target plane was put to find a conversion factor between the readings from a beam splitter and the actual delivered energy to the target through a range of attenuations. All energy measurements were done by taking the height of the peak produced by the pyroelectric sensor, and converted to the corresponding value in joules. For some optical configurations it was necessary to put a fluorescent screen at the plane of a window leading to a vacuum section of the ion source to check if all of the beam reached the target.

A number of off-line measurements were conducted to check the overall beam quality. They were done in a dedicated optics dark room on a horizontal (versus vertical on-line configuration) optical bench with higher degree of a precision and a control. The final image was magnified by a 80 mm plano-convex PVX lens and imaged by a CCD camera (Kalatel, KTC-110). The image of the final laser spot was recorded on a digital video camera recorder (SONY, DCR-PC101) via a direct feed from a CCD camera described above. A digital film then was transferred to a computer. A recorded video was broken down into a series of images, and appropriate frames analysed with a freely distributed image analyser software, ImageJ (National Institutes of Health, USA). It was possible to measure the relative intensity of each pixel, to check geometry of the beam and to check magnification for various geometry configurations (Figure 2.3). For on-line measurements the delivered laser beam burned holes on the surface of the organic matrix. The exposure times were 10–30 seconds. The results were viewed under a light microscope (Mitutoyo, FS70). Using a special software (Motic China Group Co., Ltd., Motic Images Plus 2.0ML) it was possible to capture images as viewed by the camera (Moticam, 3.0 megapixels Motic China Group Co., Ltd.) and store them on a local hard drive. The software also allowed to measure a separation between two points. A separate calibration was

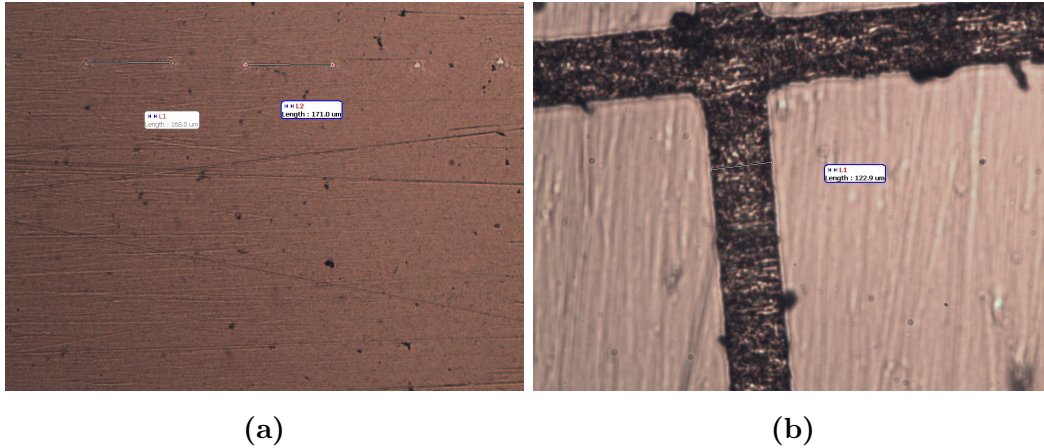


Figure 2.5: Not calibrated size comparison at the same magnification: a) $10\ \mu\text{m}$ burn marks created with a fibre optic set up, b) 200 lines/inch Nickel grid. Knowing the size of the grid it is possible to calibrate the size of the burn hole.

necessary to convert the software’s internal scale into an actual size. We used a fine grid of a well-defined size. We measured the separation between individual grid lines using a software’s line tool and calculated a conversion factor that relates a software’s scale to the real size of an image for any given magnification (Figure 2.5). The on-line measurements included exposing the target to a UV-laser for various times. A raster program allowed us to experiment with the raster velocities. Different attenuations were used to check if the spot size was energy dependent. The optimal parameters and energy range were chosen for each optical set-up. We also found that both fibre and fibre-less set-ups produced an unusual three-lobe pattern on the surface of the target, resulting from a combination of laser, fibres modes and interference (Figure 2.6). A raster line smears the lobes into a single line, as long as the step between two different lines is less than the size of the burn mark. In the case of fibre, mechanical twisting stabilized the reproducibility of the three-lobe pattern, as was shown to happen with larger fibres previously [63].

The shapes and the sizes of the burn marks were measured. Some troubleshooting was necessary once switching to the on-line measurements. The on-line set up involved a less controlled environment for the beam, as there were more optical components in use compared to the simplified off-line set-up. The on-line set-up produced a number

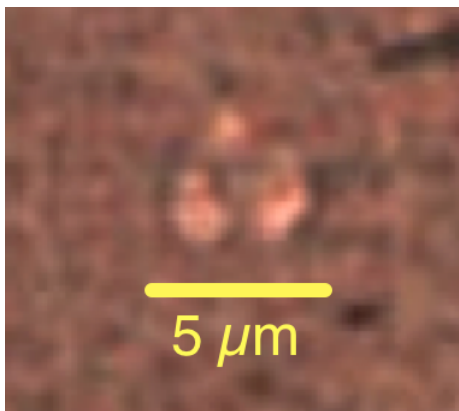


Figure 2.6: Reduced exposure of the fibre beam showcasing an unusual three-lobe structure.

of artifacts that were necessary to eliminate. These artifacts were manifested mostly as the rings around the burn marks (Figure 2.7). Both CCD camera and light microscope measurements helped to visualize the problem. A number of diaphragms and pinholes inserted in various locations, between different optical components helped to eliminate these artifacts and a permanent solution was incorporated. As a result, several of the optics holding devices had to be painted matte black to prevent the beam reflections off of shiny metal surfaces that ultimately lead to complete artifact elimination.

Ion Source Assembly

A vacuum section hosts a target holder, a stainless steel target, a cooling gas line and the steering ion optics. A schematic of the vacuum section of the ion source is shown in Figure 2.8. A target is positioned in such a way, that an incoming laser beam will have a normal incidence, making the size of a beam cross-section as small as possible. A usual MALDI instrument has a 30° or higher incidence angle, making even the smallest spot elongated in one dimension. The target is mounted on top of the two motor stages to raster in two dimensions. The motors are programmable with custom software. A UV fused silica window is mounted in the channel as deeply as it is physically possible without obstructing either a camera's view, or the ion beam

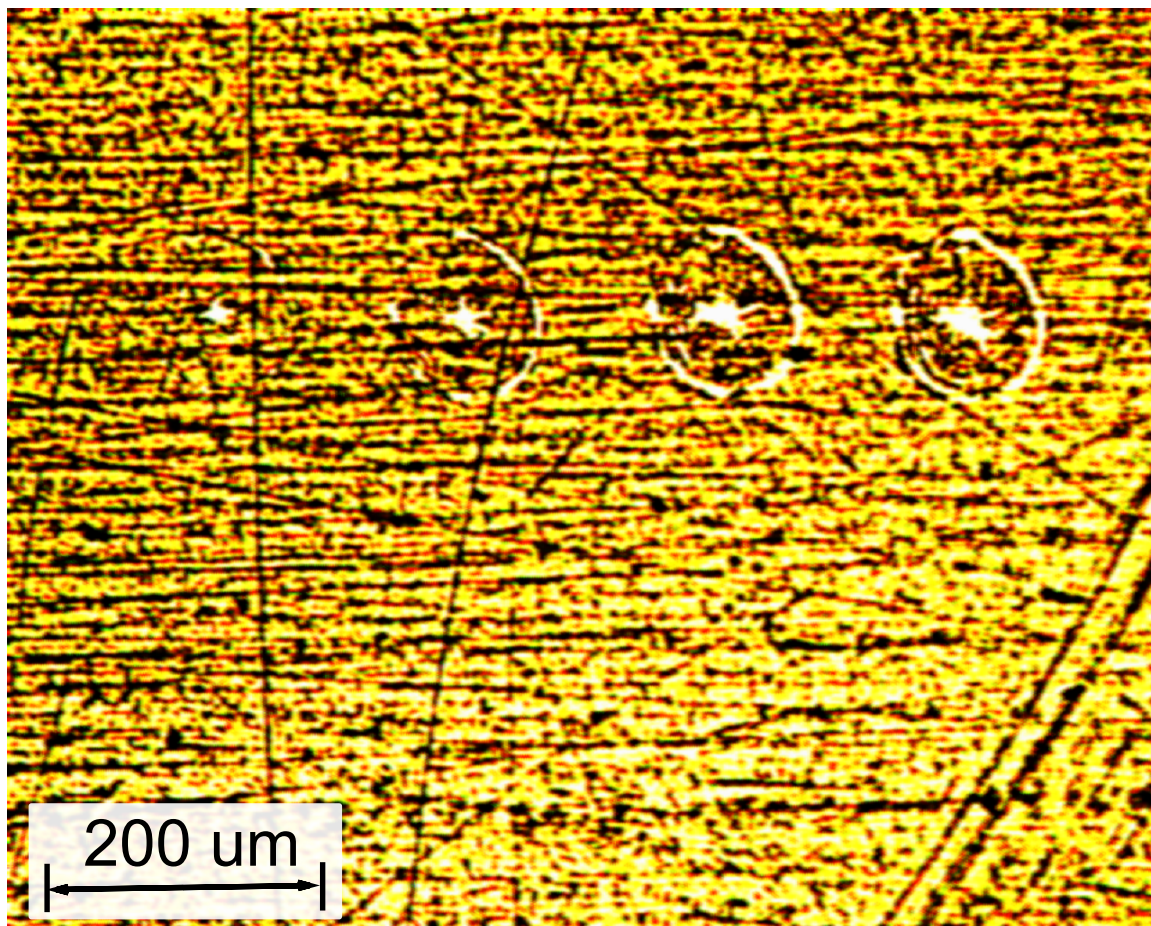


Figure 2.7: Circular artifacts found around the burn marks. The yellow background represents a layer of organic matrix.

flow. This way a final optical lens was placed as close to the target as possible.

A brass assembly is located between the window and the target. It has three basic functions: an introduction of a cooling gas into the first quadrupole guide, collection of the generated MALDI ions and hosting the ion optics. The internal horizontal channel was attached to a nitrogen gas line and went all the way through the vacuum section to an instrument's conical shaped skimmer. A short vertical channel allows the laser beam pass through the assembly, as well to allow the MALDI ions to access the horizontal channel. A small fused silica window capped the vertical channel to prevent ions from escaping.

The brass assembly itself consists of three electrically isolated segments. A gradi-

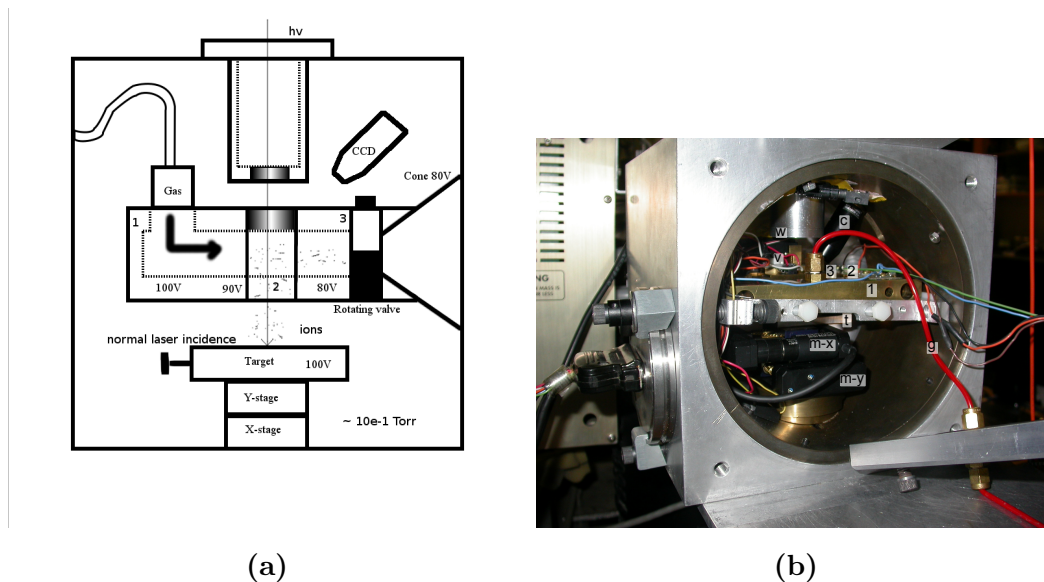


Figure 2.8: An ion source assembly: a) side view, where hv — laser beam pathway, 1 — first brass segment, 2 — second brass segment, 3 — third brass segment; b) picture, where c — CCD camera, w — window, v — rotating valve, t — target holder, g — nitrogen gas line, m-x and m-y — x- and y-axis motors.

ent across each section was applied to help ions into a first quadrupole guide. The ion source is operated in a positive mode, meaning that only positive ions are selected. The first segment was placed at 100–140 DCV, the second segment at 90 DCV and the last segment at 40–80 DCV. The potential of the target holder was the same as the first segment, the skimmer was put at the same potential as the final segment. A de-clustering potential difference exists between the target holder and the skimmer. At high laser fluences the organic matrix undergoes a volume ablation [72], trapping an ion of interest inside a huge organic cluster. The de-clustering potential difference gives the cluster enough kinetic energy to collide with a cooling gas in a first quadrupole guide. The cluster then detaches from the ion, cleaning the final spectrum and improving total sensitivity. An inherent problem comes from a large gap between the target and the brass assembly. A lot of the MALDI ions leak out due to a large pressure difference between the rest of the ion source and the area of the MALDI generation. Further improvements of the source design could improve the transmission of the MALDI ions.

The target is made out of stainless steel. It hosts a sample embedded in organic matrix. It is oriented to have a normal laser incidence. Target is removable. It is placed at a potential to help ions follow the steering ion gradient of the brass assembly. Laser beam is focused at the target plane.

The ion source also includes a CCD camera. It allows the user to monitor the laser beam location. An LED light illuminates the target to ease visual observations. A rotating valve between the ion source and a first quadrupole ion guide controls an access to the instrument. It allows the ion source to be ventilated without compromising the vacuum of the instrument. An independent roughing pump evacuates air before opening the ion source to the instrument's vacuum. A nitrogen line runs through all three brass sections for cooling of the MALDI ions (Figure 2.8a). Cooling gas is supplied from the outside of the ion source. A needle valve is used to manually regulate the cooling gas flow. The gas flow is not monitored, only the working pressures in the ion source, as well as inside the first quadrupole ion guide, where the cooling occurs. The operating vacuum inside the ion source is $1\text{--}2\times 10^{-1}$ Torr. The cooling pressure inside the first quadrupole ion guide is $5\text{--}6\times 10^{-2}$ Torr. Two ion gauges monitor the pressure inside the ion source and the first quadrupole ion guide. A small UV fused silica window caps a small vertical channel going all the way through the second brass section. It prevents the MALDI ions from leaking out and allows for the laser to pass unhindered. The third brass section couples to the instrument skimmer directly.

2.1.2 Quadrupole ion optics

The instrument has a pair of quadrupole ion guides (Figure 2.1), which are operated in RF-only mode. Their function is to provide collisional cooling and to guide ions from the ion source to the time-of-flight section. An AC voltage is supplied by a radio frequency wave generator, amplified by a set of commercial power supplies [69]. First ion guide provides the bulk of the ion cooling. The kinetic energy of ions is reduced

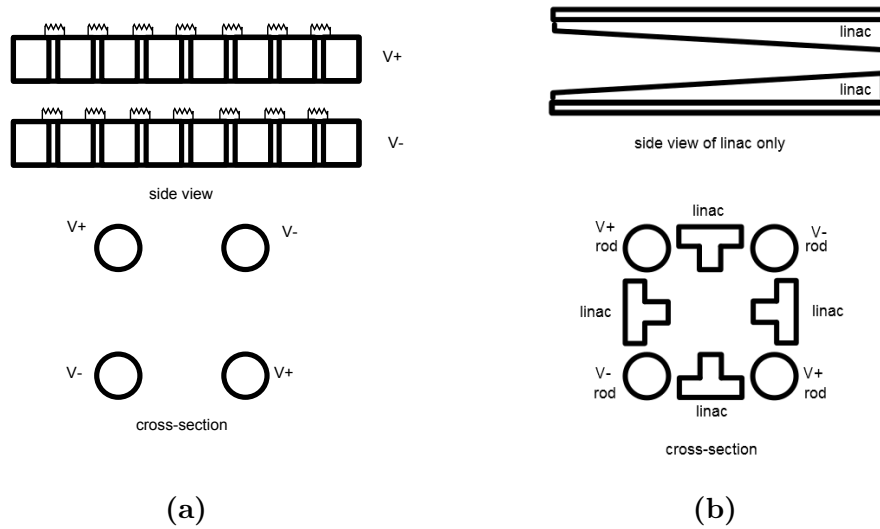


Figure 2.9: Two axial field configurations: a) conducting rings joined by the constant-value resistors and b) T-shape tapered linear accelerator.

by the gentle collisions with the nitrogen gas molecules. The gas is introduced via a gas line in the ion source. The cooling pressure is regulated with a needle valve outside of the instrument, and monitored with a DVM connected to the internal ion gauge. Second ion guide extends the ion focusing of the first quadrupole and further reduces the energy spread of ions at a lower vacuum. The ions are spread in time and shaped into a quasi-continuous beam [19].

Both ion guides have small axial fields, which reduce the ion residence time inside the quadrupoles. Two ways of field generation are employed. First ion guide consists of co-axial rings with voltages provided by a voltage divider (Figure 2.9a). Each ring is connected by the constant value resistor, establishing the potential gradient, which produces a weak axial field. Second ion guide is augmented with a static linear accelerator (Figure 2.9b). It consists of four T-shaped tapered electrodes arranged around the axis of symmetry in between the quadrupole rods [70]. A DC voltage potential is applied. The geometry of the electrodes produces an electrostatic field gradient.

When ions leave the second ion guide, they are introduced into a field generated

by a pair of deflection plates that steer them into a modulator at the right angle.

2.1.3 Mass analyser

After the MALDI ions emerge from the ion guides, they are directed into the modulator of the orthogonal time-of-flight (oTOF) mass analyser (Figure 2.1), consisting of a plate and a grid [69]. The first stage of the acceleration column is initially held at zero field to prevent field penetration. A pulse of -1 kV is applied to its grid at the same time when $+1$ kV pulse is applied to the modulator plate. The pulses have $12 \mu\text{s}$ width and the ions are injected into a DC acceleration drift column at 3 kHz frequency. The acceleration column consists of circular rings electrically isolated from each other. The entrance is at the ground, the exit is at the acceleration voltage, -10.5 kV. The rings are connected by the constant value resistors to provide a uniform acceleration field across the region. Once ions gain the kinetic energy, they are left to drift in a field-free tube isolated with a conducting sheath. During this time ions separate based on their m/z value.

An electrostatic mirror is used to improve the resolution of the instrument [12, 73]. A two-stage electrostatic mirror introduces a second-order correction to the peak broadening inherent with the use of high acceleration potentials. It consists of two regions, representing a hard and a soft deceleration segments. The ions slow down in the first mirror section, turn around in the second section and get reflected back into the field-free drift region with the same kinetic energy.

The ions eventually arrive to a detector located further down the instrument. The ions need to have a small transverse velocity to reach the detector, which can be set by the use of quadrupole ion guide acceleration gradients, and steering plates prior to ion entry into a TOF modulator.

2.1.4 Detection

The detector consists of two micro-channel plates (MCPs) oriented in a chevron configuration. The resistance across each MCP is 15 M Ω , making a total resistance across the detector 30 M Ω . Two plates are connected to each other with a conducting ring. The detector floats at the acceleration potential with a 2 kV potential difference across two MCPs.

When the ions hit the first MCP, an electron cascade results that strike a second plate. The second MCP amplifies the electron cascade further. An anode collects the amplified signal generated by the second MCP. To improve the dynamic range of detection, the anode consists of four independent nodes. If two similar hits happen relatively at the same time on different nodes, both hits can be registered. The anode transfers the amplified signal to a discriminator. Pulses below a certain threshold are discarded to reduce the spectrum noise. The signal is then transferred to a multi-stop, 4-input time-to-digital converter (TDC).

The TDC is a digital stopwatch. When an acceleration pulse is applied in the modulator region of time-of-flight mass analyser, a signal is sent to TDC to start the clock. Once ions arrive to a detector, the stop signals cause the measured time to be stored. The TDC then takes a difference between two time stamps and sends the result to a custom software, *tofmulti*. It converts the recorded time into an m/z value,

$$\sqrt{m/z} = A(t - t_0) \quad (2.7)$$

where A, t_0 are the calibration parameters, t is the arrival time of the ion [69]. TOF spectra are linear with respect to time, therefore the instrument can be calibrated with a straight line. A is the slope of the calibration line, t_0 is an offset of the arrival time. Our spectra were calibrated using a two-point calibration, including dalargin (726.4 Da), and melittin (2845.8 Da). *Tofmulti* remembers calibration parameters and automatically calculates m/z value from the measured time.

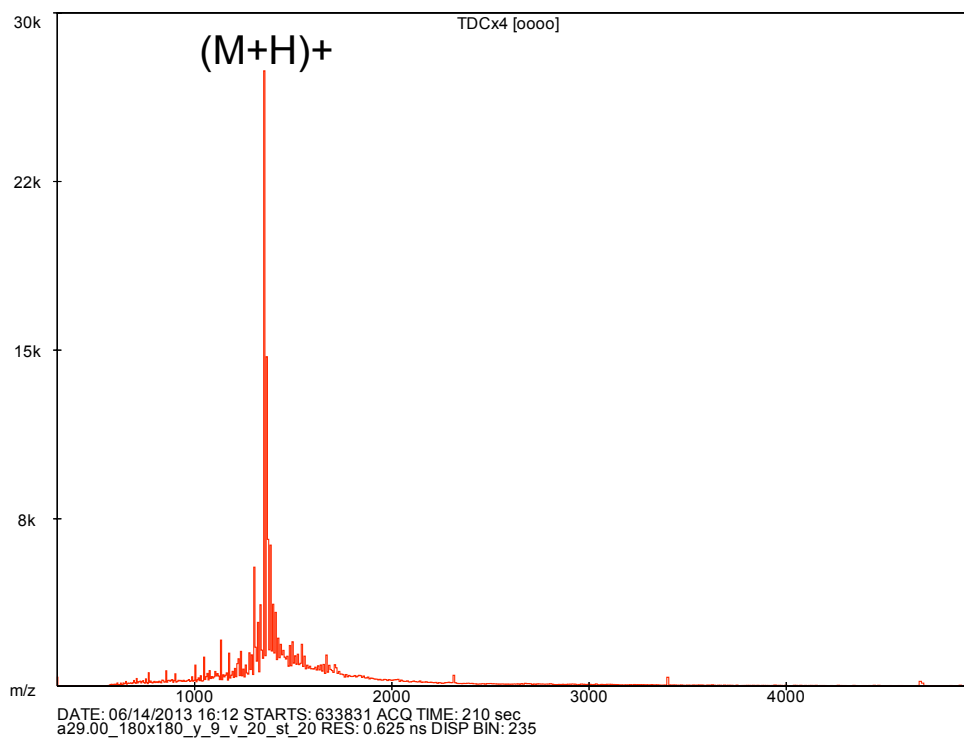
The ion counting method described above differs from the usual analog system employed in axial TOF instruments, where typically more than 10^4 ions are recorded in a transient by an analog-to-digital (ADC) system in a digital oscilloscope. This has the advantage that many more ions can be recorded in a single injection. However, in an orthogonal system the ions from a single laser shot can spread in a quasi-continuous beam; a much higher injection rate means only a few ions are injected at a time. Digital counting methods have lower electronic noise, better dynamic range and potentially better time resolution, and do not suffer from detector saturation.

2.2 Sample Preparation

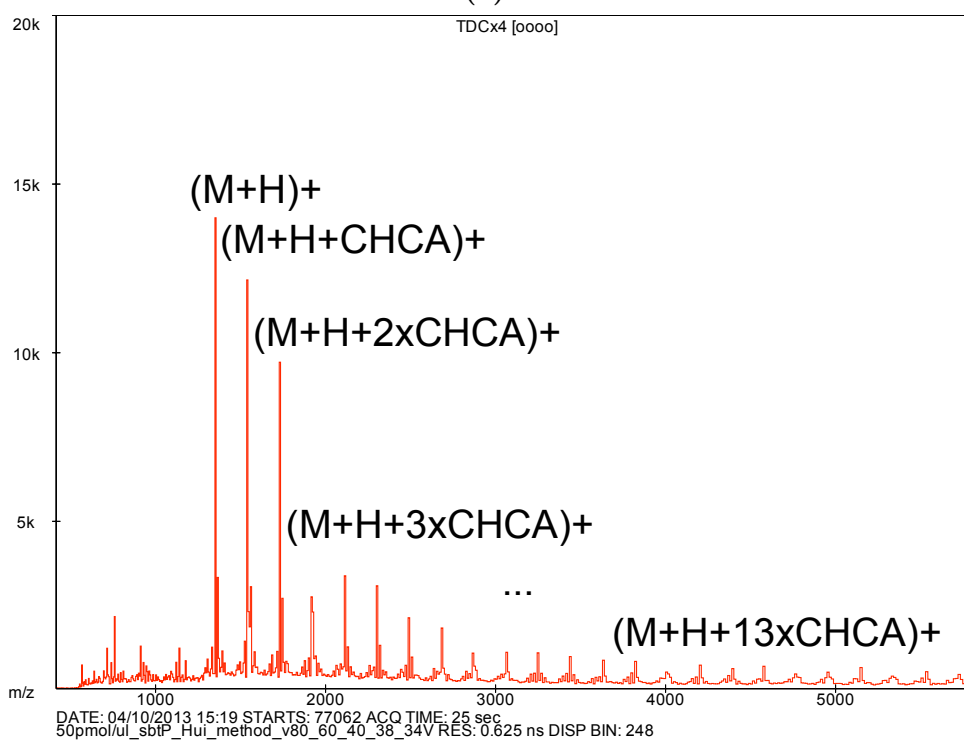
2.2.1 Sample and matrix preparations

Sample. We chose the Substance P (Sigma, 98% purity) to be our sample. Its sequence is Arg-Pro-Lys-Pro-Gln-Gln-Phe-Phe-Gly-Leu-Met-NH₂, 1347.63 Da. Its mass spectrum consists of a parent isotopic pattern ((M+H)⁺) (Figure 2.10a). No signal suppression accompanied by more complicated mixtures is observed [53]. On the spectra the intensity of Substance P peaks appears to be relatively resistant to changes in cooling pressure, although the clusters will still occur if not enough of de-clustering energy is given to the MALDI ions between a target and an instrument's skimmer (Figure 2.10b). Substance P is easy to prepare and to use. Substance P was dissolved in 0.1% trifluoroacetic acid (TFA) solution to a concentration of 50 pmol/ μ l. Lower pH solutions modify peptides by adding positive charges on certain amino acids that make hydrophobic species more soluble in water or other hydrophilic solutions. The presence of TFA or a formic acid is preferable when trying to incorporate peptides into a matrix crystal [74].

Matrix. When choosing a matrix, we were looking for a compound that would create small topological crystals. α -Cyano-4-hydroxycinnamic (CHCA) acid was used



(a)



(b)

Figure 2.10: Substance P: a) a typical spectrum; b) a typical spectrum with matrix clusters.

as an organic matrix of choice. It is one of the popular matrices in use, others being 3,5-dimethoxy-4-hydroxycinnamic acid (sinapinic acid) and 2,5-dihydroxybenzoic acid (DHB). DHB is routinely used in protein analysis. Although its use is ubiquitous, DHB creates large crystals, on the order of hundreds of micrometers [75]. Sinapinic acid creates small crystals, but it tends to inhibit the peaks below 2000 Da, and largely used for high m/z -value compounds. We used CHCA to develop a homogeneous deposition method. It creates small crystals (1–2 μm), and it does not inhibit the signal the way sinapinic acid does. It is a matrix widely used in imaging mass spectrometry techniques, because with proper deposition techniques, it minimizes sample migration. However, it has a high proton affinity, so it competes with the analyte for ionization. CHCA is easy to handle. We used a saturated solution of CHCA in 50% acetonitrile (ACN).

The matrix and the analyte are mixed together. The search for the proper ratio between analyte and the matrix concentrations is necessary to avoid the cluster formation, as well to improve the overall intensity of the parent peak. Literature suggests mixing matrix with analyte in 50000:1 molar ratio. If mixed evenly, this ratio will embed an individual analyte molecule inside a matrix lattice, and separate it from other analyte molecules. The matrix lattice will absorb most of the UV energy delivered by the laser beam, protecting the analyte from fragmentation. After the phase change, the primary ionization reactions will take place, and ionize matrix. The ionized matrix will induce charge on the analyte inside the plume via the secondary reactions. However, if an over-abundance of the matrix molecules exists, matrix will compete with the analyte molecules for secondary ionization reactions, leading to a decrease of supply of the analyte ions. CHCA has the highest proton affinity out of the three matrices mentioned above. As a result, the chemical noise will be visible in the spectrum. A chance of creating matrix adducts will also increase, leading to creation of clusters. The appropriate steps were taken for each deposition method, and clusters were removed by varying the atmospheric conditions inside the source

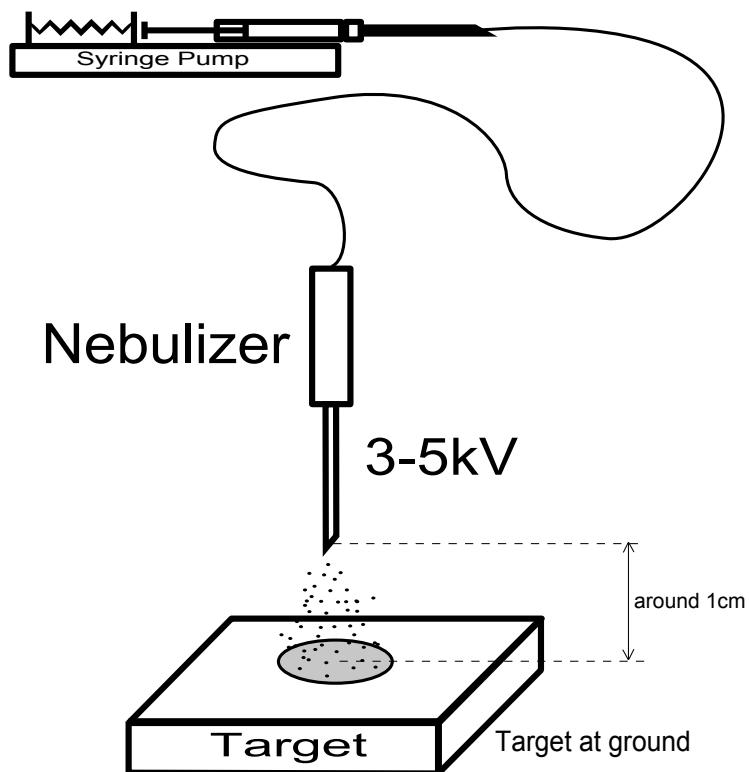


Figure 2.11: Electro spray deposition system. It consists of a syringe pump, a tubing, a nebulizer connected to a high power supply and a target at ground.

and the first quadrupole ion guide, as well as introducing a de-clustering potential between a target and the instrument's skimmer.

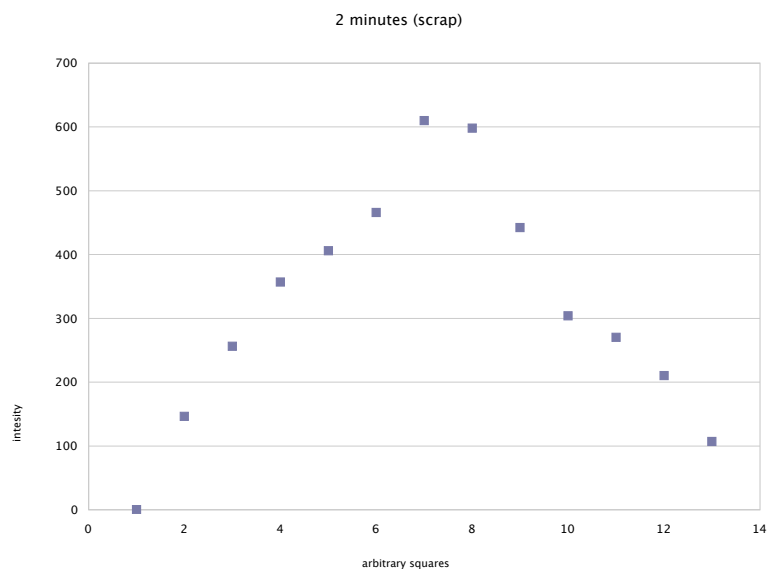
2.2.2 Deposition methods

To compare ion sensitivity from different experiments, it is necessary to produce a flat signal response across the deposited sample. We compared three different deposition methods: electro spray deposition, one-layer spotting and two-layer spotting. Only the two-layer spotting was used as a sample preparation in the experiment.

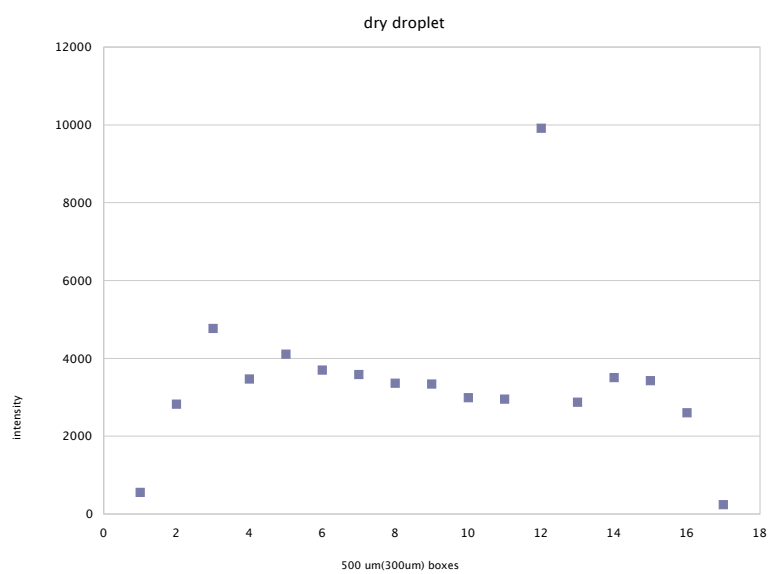
Electrospray deposition. In order to produce a homogeneous layer of matrix mixed with the analyte, the electro spray principle was employed (Figure 2.11) [76]. 50 pmol/ μ l of Substance P in water was mixed with the saturated CHCA in methanol.

Pure methanol was used to facilitate the evaporation process, as well as to lower the operating high voltage range. The mixture was loaded into a syringe pump that operated at 50 $\mu\text{l/hr}$. The syringe was connected to a needle (0.24 mm inner diameter, tapered tip) via a small diameter short tubing. The needle was connected to a variable high voltage power supply. Together they formed a nebulizer, a device responsible for converting aqueous sample into a gas phase. The nebulizer operated at room temperature and in atmosphere, the power supply provided a 3–5 kV direct current voltage. The distance between the nebulizer the target surface was around 1 cm. The target was at ground. A CCD camera was positioned on the side (not shown) to monitor the cone of the aqueous sample. At the tip of a nebulizer, the sample is completely surrounded by a layer of positive charges from the solution provided by the high voltage power supply. As the sample evaporates, it undergoes constant division and segregation due to ionic charge. As sample splits into smaller droplets, a phase change, from liquid to gas, occurs. Once in a gas phase, sample molecules experience a strong electrostatic field and follow the field lines towards the target surface. The sample is then deposited on the target's surface in a thin layer. With the use of the CCD camera and fine-tuning the power supply, it was possible to achieve the arrival of the semi-wet sample on the surface of the target. Wetness was necessary for the matrix to surround our analyte in order for the MALDI process to occur. The average time of deposition was around 1 hr. The size of matrix crystals is expected to be 2–4 μm [76].

Although the film we produced was thin, it could only be used as a test for the size of the burn mark. Our experiment required an even signal output from a relatively large area. Since the electric field lines are not parallel to each other in this configuration, more of the sample was deposited closer to the needle. The amount of deposited material quickly decreased outward and the amount of signal extracted from this method varied (Figure 2.12a). Even though electrospray could produce very thin films, the signal was not even across the spot. It is possible to improve



(a)



(b)

Figure 2.12: Signal from $500 \times 500 \mu\text{m}^2$ squares along the axis of symmetry of a spot by a) a 2 minute electro spray deposition; b) a two-layer spotting.

the uniformity by moving the sample during electrospray, but this would increase the deposition times to several hours, which is impractical.

One-layer spotting. One of the suggested methods to produce a homogeneous spot is to use a fast-evaporation spotting [77]. The method involves the use of volatile solvents, such as acetone, to quickly deposit a thin layer of matrix. The solvent dries out quickly, leaving a thin film of the matrix over a large surface area. We mixed both analyte and the matrix as our sample using acetone, methanol and acetonitrile in various concentrations as a solvent. 1 μl of the sample was deposited on the surface of a stainless steel target, and a thin film was produced. However, the quality of the film was unacceptable for all of the solvents. Matrix crystals formed small colonies, clumped together across the spot surface. The colonies were unevenly distributed, with large gaps in between. The size of the matrix colonies and the gap size varied with the solvent in use (Figure 2.13). Acetone dissolves more matrix than methanol or acetonitrile. Methanol dissolves more matrix than acetonitrile. It can be seen from the figure that the surface density of the matrix crystals decreases in the order of acetone, methanol and acetonitrile. Addition of water decreases homogeneity of the matrix film and the solubility of the matrix. 100% Acetone and methanol produced the best results, with acetone taking the least amount of time to dry. Methanol produced more even crystal deposition. This can be accounted for matrix having time to distribute itself more evenly during a longer evaporation time of methanol. Acetonitrile dissolved matrix poorly, creating larger crystals in uneven patch pattern.

Two-layer spotting. Upon further examination we found that both acetone and methanol would distribute itself in such a way, as to fill in smaller imperfections and scratches of the stainless steel target. Polished target surface provided an uninhibited spread of the sample, creating large holes between the matrix colonies. We then switched to targets with rougher surface to prevent the spread of a volatile solvent. To further make a solvent behaviour more predictable, we deposited one

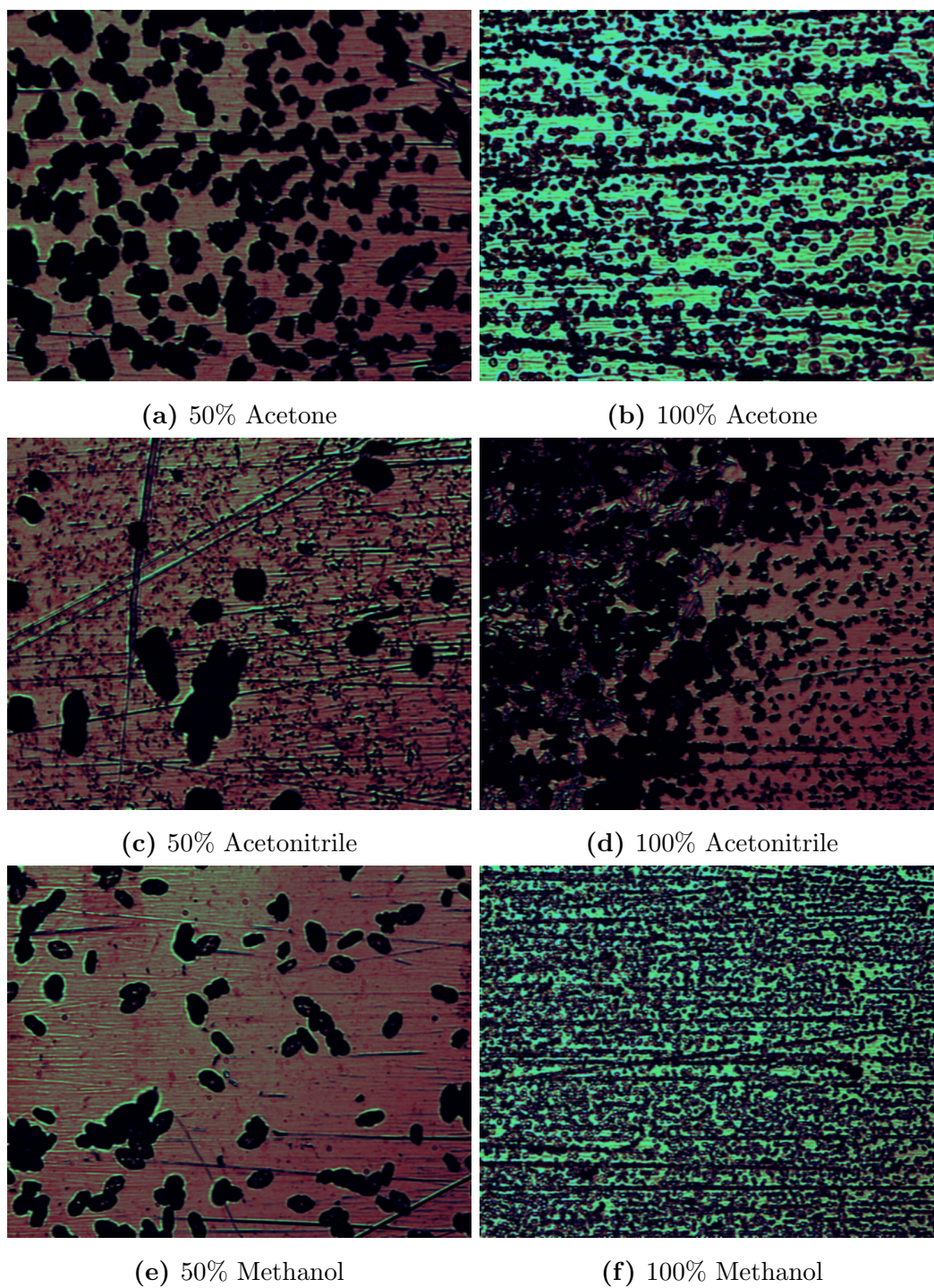


Figure 2.13: Relative size of the matrix crystals using one layer spotting technique with different organic solvents.

layer of matrix dissolved in pure acetone to provide an even background layer for the second spot. To take advantage of slow evaporation of acetonitrile and water, we used 50% ACN solvent to mix matrix and sample together. Simply adding analyte to a first layer resulted in a poor analyte incorporation, and a decrease in overall signal. Second solvent is a less hydrophobic solution preventing dissolving of the first layer due to difference in the matrix concentration. While drying, the analyte and the matrix have time to mix and distribute themselves evenly. As a result, we produced spots of an area 3.6–3.8 mm² that provided even signal responses across their surfaces (Figure 2.12b). The signal variation was within 20% considering all data points, and within 10% removing one point in the middle and signal from the edges, as expected [78, 62]. We chose this method of deposition to ensure reproducibility of the signal. The layers of the matrix and the analyte were also evenly distributed, as can be seen in Figure 2.7.

A number of deposition techniques produce homogeneous deposition of matrix, but not all provide proper integration of the analyte inside the matrix crystal. DHB deposition via pneumatic system or sublimation can produce even films and small crystals, but do not integrate peptides and proteins properly, leading to a decreased ionization efficiencies. However, sublimation and pneumatic deposition work well with lipids.

2.3 Data acquisition and analysis

Mass spectra were acquired with software, *tofmulti*, developed in-house. The ion signal was measured by integrating the area of the parent peak. The MALDI ion yield from a single spot of the size of a few micrometers is small, and moreover, the actual size of the spot, and in particular the amount of area damaged, is difficult to determine. Therefore, instead of irradiating one spot, the laser rastered over a rectangular area (by moving the target) and the signal was integrated (Figure 2.14a).

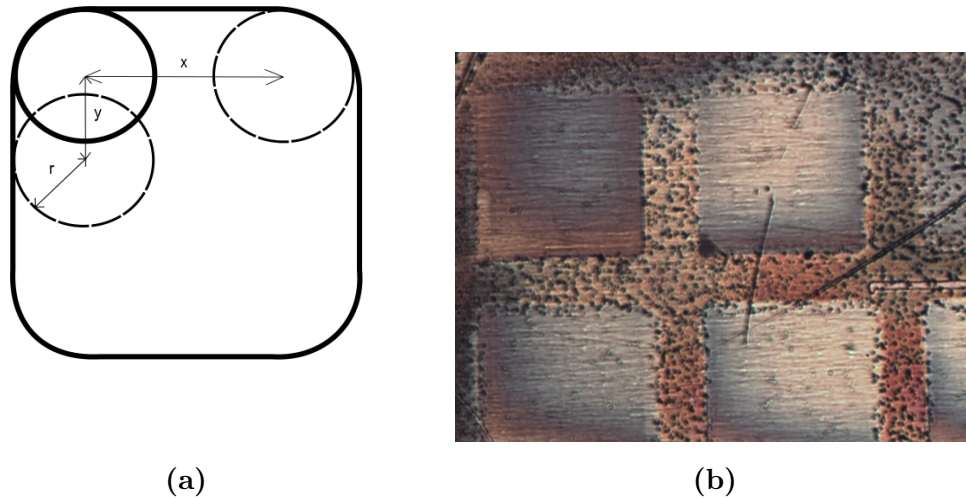


Figure 2.14: a) a schematic of the raster program, where r — the radius of the laser beam, x — the size of the raster line, y — step size; b) a light microscope image of a $310 \times 310 \mu\text{m}^2$ resulting scan.

Each raster line has a length, x , usually between $200 \mu\text{m}$ and $500 \mu\text{m}$. The laser beam was scanning across the target surface at speed, $v = 20 \mu\text{m/s}$. Once the beam has reached the end of the raster line, the x-axis motor reverted to the beam's starting position, and the y-axis motor moved the target perpendicularly a step distance, y . The raster line and the step sequences repeated again until the total shape of the irradiated area became a square. The effective spot size was verified under the light microscope by measuring the total size of the irradiated area, and then subtracting from it the programmed parameter x . The difference results in the diameter of the beam size, $2r$. The step size, y , and the velocity, v , were optimized by repeating an experiment until the set of values was chosen that yielded the strongest ion signal. The raster line length, x , was calculated to finish the scan within 3 minutes. While the raster program was running, all of the signal was collected into a single spectrum. The total signal came from the whole irradiated area. We normalized the signal by dividing it by the total irradiated area of the scan program. The normalized result was then used for plotting the dependence of the total ion yield versus energy.

The energy of the laser beam was measured as previously discussed. The energy coming out of the fibre has a flat-top profile [63]. The fluence can then be calculated as energy divided by the area of the laser spot size. However, the Gaussian beam energy has a radial dependence, so the average energy is used when estimating the fluence of the laser beam spot [67]. For our purposes, we varied the laser energy greatly, leading to larger effective spot sizes at higher energies. Since we could not keep the effective spot size constant, we chose to track the total energy contained inside the spot instead. We used a total energy of the laser spot in our total ion yield profiling instead of the laser fluence. The theoretical fluence was calculated as necessary.

Chapter 3

Results and Discussion

Previous investigations of spot size dependence typically report ion yield per shot or sensitivity as a function of fluence or as a semi-logarithmic plot [66, 63, 65]. As described in the introduction section, ion yield per shot has a power law dependence on the laser fluence. The number of ions produced rapidly increase with increasing fluence until the saturation point. Saturation occurs when the number of ions produced cannot be increased by increasing laser fluence. At this stage various fragmentation processes start to compete with the ion production. It was shown that for fluences below saturation the ion yield per shot follows a cubic dependence on the irradiated area, leading to an early impression that smaller spots produce overall less ions and are therefore less viable. However, recently the total ion yield per unit area (sensitivity) was studied [63]. Qiao *et al.* showed that by decreasing the laser spot size it is possible to raise the saturation point. The ionization efficiency increases with smaller spots and higher laser fluence. Above saturation fluence, levels sensitivity (as well as ion yield) has a *linear* dependence on the area of the spot. Since saturation occurs at high fluence, better sensitivity can be achieved with smaller spots, despite lower total ion yield per shot.

Previous research involved the use of laser spots, 200 – 10 μm in diameter. The goal of this experiments is to see if even smaller spots provide any practical use for

fibre and fibre-less geometries. The results of our experiment are presented as a sensitivity measurement. Three experiments were performed in order to understand how sensitivity performs for the laser spot size below $10\ \mu\text{m}$ and high energies. Fibre and fibreless geometries are employed at 1-to-1 and 2.4-to-1 magnifications for comparison.

3.1 Fibre optics

To define a reference point in sensitivity measurements, $10\ \mu\text{m}$ fibre was imaged in 1-to-1 configuration as depicted in Figure 2.2a. The size of the laser spot was confirmed via CCD measurements and via burn mark analysis with light microscope. As previously reported, the beam exhibits a speckle pattern produced by laser modes and interference. Our beam shows a pattern resembling a three-leaf clover, each is one third of the size of the overall spot size.

Coupling the laser beam to an optic fibre becomes increasingly difficult for small diameter fibres. The size of the focused beam with our optics is $24\ \mu\text{m}$ versus $10\ \mu\text{m}$ fibre. A lot of energy is wasted, leading to a lower fluence range. The energy measurements are barely possible to make. The beam could be focused to a smaller spot, but thermal degradation of the fibre limits the total energy. As the fibre is used in the experiment, which takes between 3 and 10 minutes of continuous use, its tip heats and melts. The high fluence focused onto the plane of the fibre entrance causes its transmission to decrease.

We produced a $3\text{--}4\ \mu\text{m}$ laser spot using 2.4-to-1 geometry (Figure 2.2b). The beam profile and spot size were confirmed using CCD camera and matrix burn mark analysis. The beam profile is similar to a $10\ \mu\text{m}$ fibre, with speckles of $1\text{--}2\ \mu\text{m}$ diameter each. Some energy is lost between a fibre and an object plane due to larger separations between the first aspherical lens and a fibre, but the fluence is increased due to smaller spot size. The same laser coupling problems encountered with $10\ \mu\text{m}$

fibres hold with new optic configuration.

The results are comprised of the sensitivity (an intensity of Substance P parent peak divided by the raster area) and the energy or the fluence measurement. Due to wear of the optical fibre, as well as the time length of each measurement, it is difficult to construct a full sensitivity versus fluence profile. Flucose measurements are problematic due to energy transmission dropping over time. The average energy can be approximated by measuring starting and final energy output for both geometries. Due to unpredictable decay in transmission, the fluence can only be reproduced with a fresh fibre. The energy output of 10 μm fibre is low as is, so with a lowered transmission the energy readings are problematic, even though the ions are detected in mass spectrometer. As a result, we report sensitivity measurements at near the optimal fluence for 10 μm and 3–4 μm spots.

Looking at sensitivity measurements alone (Figure 3.1), some conclusions are possible to make. The sensitivity continues to increase with smaller laser spot sizes. The 3–4 μm spot showed greater sensitivity over 10 μm spot. This means that there were more ions created per unit area for smaller spot than for larger spot. The fluence used is at the saturation point. As the fluence increases, the number of ions gradually decreases due various fragmentation processes. A greater sensitivity was achieved for the same energy output from the fibre just by focusing laser to a smaller spot.

There are differences between Qiao's *et al.* and this work. Qiao made single spot sensitivity measurements by consuming all of the matrix. Total number of ions generated from sub 10 μm spot sizes is small and spot size estimations are difficult, so that method does not work for us. By scanning a rectangular area, more ions are generated improving statistics, the irradiated area can be accurately determined independent of the speckle pattern, and moreover it is more representative of a practical imaging experiment.

The scan-box size varies between $200 \times 200 - 500 \times 500 \mu\text{m}^2$. The raster speed is 20 $\mu\text{m}/\text{s}$ leading to somewhat lengthy acquisition times, which usually leads to fibre

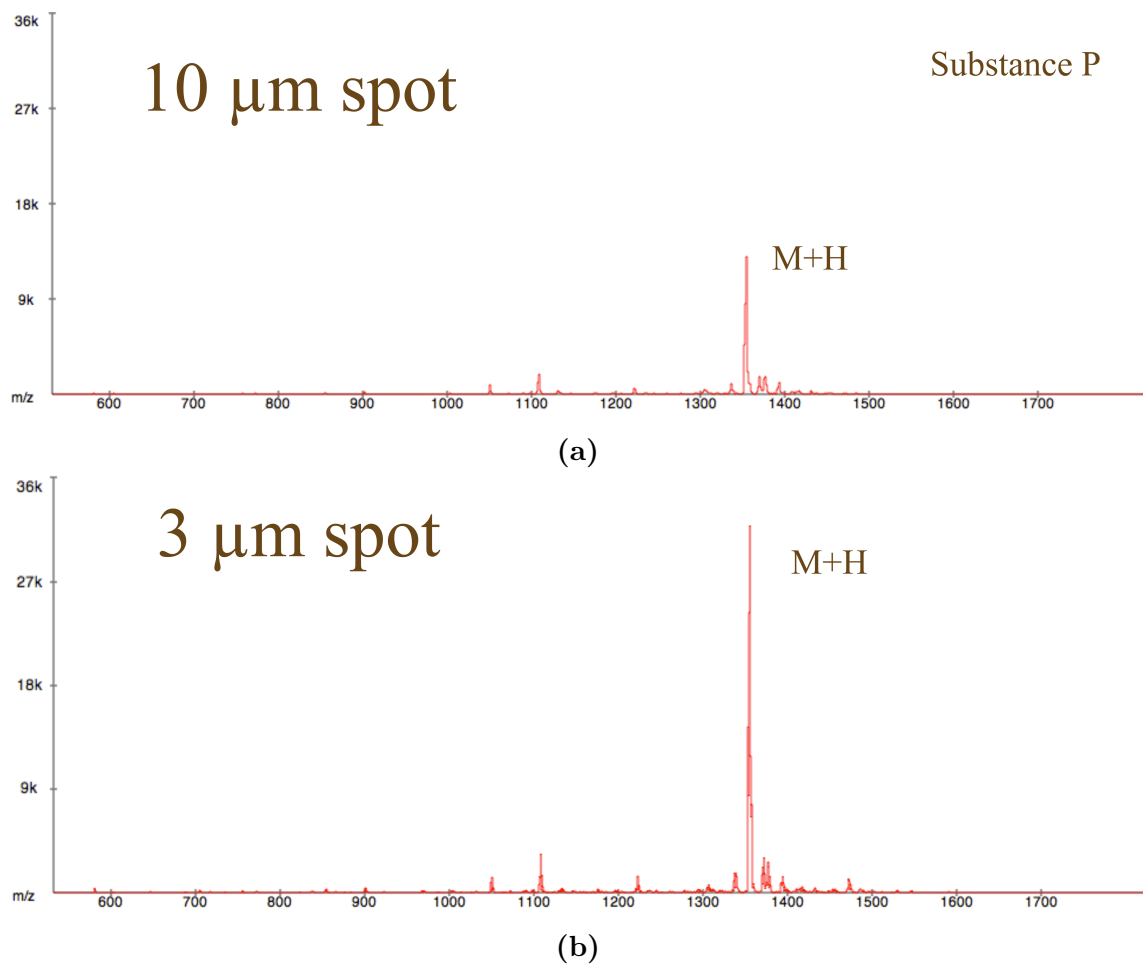


Figure 3.1: Total ion yield generated by scanning $310 \times 310 \mu\text{m}^2$ area with a) $10 \mu\text{m}$ and b) $3\text{--}4 \mu\text{m}$ laser spot.

damage. This introduces a large cumulative error in estimating a total ions generated. The measurement readings become an average result for a range of fluences, which can vary by 40% per line over the course of the run, which is not practical. Energy readings are hard to make for small fibres due to coupling issues. We can only approximate the starting fluence of the run. Using a geometry argument, the fluence of $3\text{--}4 \mu\text{m}$ spot is twice than the fluence of $10 \mu\text{m}$ spot. We can conclude however that the starting fluence is above the saturation point. The degradation of transmission for two geometries is similar, as the same laser-fibre coupling method is used. The results can be compared to each other if the raster program is the same.

Nonetheless, our results show that the sensitivity increases with a smaller spot size

and an increased fluence. Although this particular method carries a lot of problems with energy coupling, energy measurements and comparison to previous work, the two geometry configurations create two points of reference with statistical confidence to extend previous findings to sub 10 μm laser spot size. As the fluence decreases, we can only speculate if the sensitivity follows previously established trends [63, 66, 65].

3.2 Fibreless optics

The use of fibre optics as described above allows a separation of the effects of fluence and spot size, but thermal damage makes it impractical for long runs typical of imaging experiments. We have therefore attempted to measure sensitivity using fibreless optics. In this case, the fluence distribution at the target is Gaussian-like, so the effective spot size is not easy to define [67]. In particular, because of the steep dependence of the yield on fluence, at high fluence, the effective spot size can be many times larger than the full-width at half maximum (FWHM). However, since the spatial resolution in imaging experiments is often limited to tens of μm by sample preparation, we were interested in whether spot sizes with small FWHM would still improve sensitivity even at high fluence, where the effective desorption area is considerably larger. That is, for practical purposes, with optics designed to produce $\sim 5 \mu\text{m}$ spots (FWHM), but with a much larger effective spot size at high fluence, is there still an improvement in overall sensitivity?

A short focal length lens is used to produce a small spot of a few microns. This spot is then imaged either in 1-to-1 or 2.4-to-1 geometry. Although there are energy losses due to the lens size, a larger amount of energy is possible to deliver to the target plane. The energy channelled into a spot of 5 μm spot is at least twice as large in fibreless geometry than in optic fibre configuration of the same spot size.

The spot size is measured using the matrix burn mark analysis. As mentioned earlier, the laser spot size depends on the channelled energy with the smallest mea-

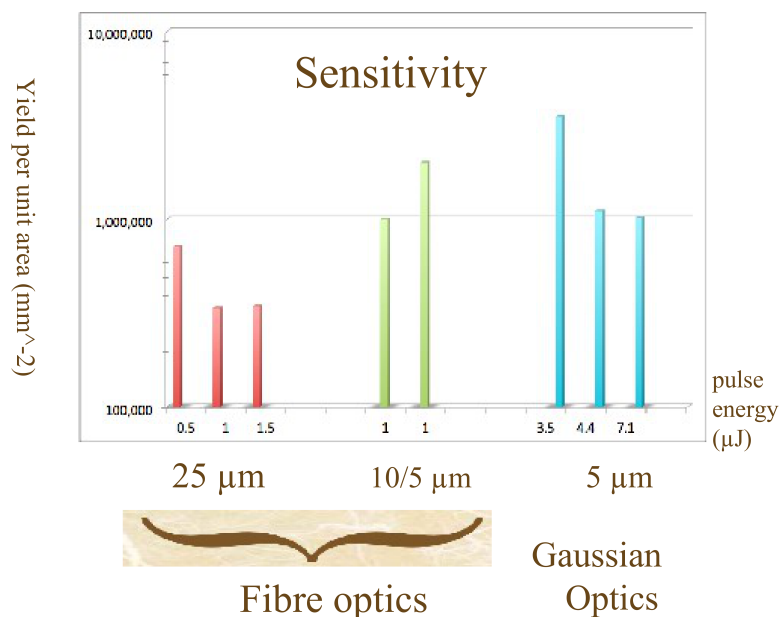


Figure 3.2: Comparison of sensitivity results for fibre optics (25 μm and 10 μm spot size) and fibre-less optics (5 μm spot size).

surable spot size at the lower range of energies. Spot size also depends on the local matrix topology. Target surface is rough by design to prevent the first layer of matrix from spreading out. Some areas are thicker than others, even though an even signal output is produced. Due to angular spread of the beam, the depth of focus is small for two geometries in use, leading to laser spot size variation for thicker matrix areas. Nonetheless, the smallest measurable spot sizes are on the order of 3–5 μm diameter. At lower energies it is difficult to discern the spot size of the beam, even though the ions are produced and detected. In those cases we suspect that the laser spot is smaller than 3 μm , and not all of the matrix is consumed during the irradiation.

Raster program was set to completely ablate a $300 \times 300 \mu\text{m}^2$ area in one run. The highest sensitivity was observed for a laser energy of 3.5 μJ (Figure 3.2). It was difficult to estimate the ablation area leading us to believe that some, but not all of the matrix was consumed during the raster program. A 25 μm fibre raster data was used to compare the results.

The energy in fibre-less configuration can be measured effectively. The range of energies is an order of magnitude larger than in fibre optics of the same magnification

geometry. At this configuration only the profiling at the saturation levels is possible. An expected decay in sensitivity as the laser energy goes up is observed. It is necessary to bring the energy below the saturation point to meaningfully profile the sensitivity.

When looking at the sensitivity, fibreless configuration shows similar results to the fibre optics for the same area of ablation. The energies in both cases are above the saturation point, where the sensitivity starts to drop off. The shoulders of Gaussian-like beams operate at lower energies than the middle part. At larger energies the effect of hysteresis becomes noticeable. Shoulders of Gaussian-like beam modify neighbouring matrix molecules. Highest sensitivity was achieved with smaller spot sizes and higher energies. When comparing to a 25 μm fibre data, fibreless optics with smaller spots generates higher total ion yields per unit area. As the energy goes up, the size of the spot and the hysteresis effects increase leading to a decreased sensitivity.

3.3 Sensitivity profiling

In the preceding sections, the sensitivity was measured at only one or two different values of the fluence, because of difficulty in prolonged measurements with small fibres. The sensitivity profiles as a function of fluence for a variety of fibres were reported previously by Qiao [63], and are expected to be the same in this experiment. However, for Gaussian-like beams, the profiles of the sensitivity is not necessarily expected to follow the same trend. As the laser pulse energy is increased, the fluence increases proportionally, but because of the Gaussian-like behaviour, the effective ablation area increases as well. Moreover, there is a hysteresis effect with some matrices [79] wherein irradiation at a certain fluence can modify the surface inhibiting further ablation, even at somewhat higher fluence. Therefore, for Gaussian-like beam spot rastering a surface, the tails of the distribution irradiate the surface first, so there is a competition of the effects of higher fluence, larger effective spot size, and hysteresis. We therefore undertook to measure the dependence of sensitivity on fluence for at

least one fibre-less configuration to determine from a practical point of view what the optimum pulse energy is. Note that the effective spatial resolution is degraded at higher fluence because of the larger spot size, but in many cases, the spatial resolution is limited by sample preparation.

The sample translation stage has a rather critical spacing between the target and the opening to the ion transport cell, and during the measurements reported in the previous two sections, binding problems forced a complete rebuild of the sample assembly to increase that spacing. Unfortunately, the effect of this was to decrease the instrument transmission by about an order of magnitude, presumably because ions were lost as a result of gas flow through this spacing. This lower (and erratic) transmission meant that the absolute sensitivity should be regarded with some caution, although, presumably the profile is still informative. Two profiles were obtained with fibres, but because of the lower transmission, only larger fibres of 50 μm diameter gave enough signal.

The sensitivity profiles for fibre and fibre-less configurations are reported in Figure 3.3. The 1.27-to-1 magnification was produced by separating two aspherical lenses (d in Figure 2.2). The fibre optic configuration produces flat-top beam profiles for which it is easy to calculate fluence. The laser spot sizes for an optic fibre at 1.27-to-1 and 2.4-to-1 magnifications are 40 and 21 μm respectively. The sensitivity of smaller spot is slightly higher than for the larger spot (Figure 3.3a). This can be explained by the fluence of 21 μm spot size being 4 times higher than the fluence of the 40 μm spot size for a given energy.

For fibreless measurements laser was directly imaged with the 3-lens configuration, however this particular configuration produces a Gaussian-like beam. We plotted sensitivity with respect to an average fluence, calculated from the energy per pulse divided by the smallest effective spot size (approximated FWHM). The smallest effective spot size in fibreless configuration is 3–5 μm .

Our reference data shows that the sensitivity improves for our geometry just as

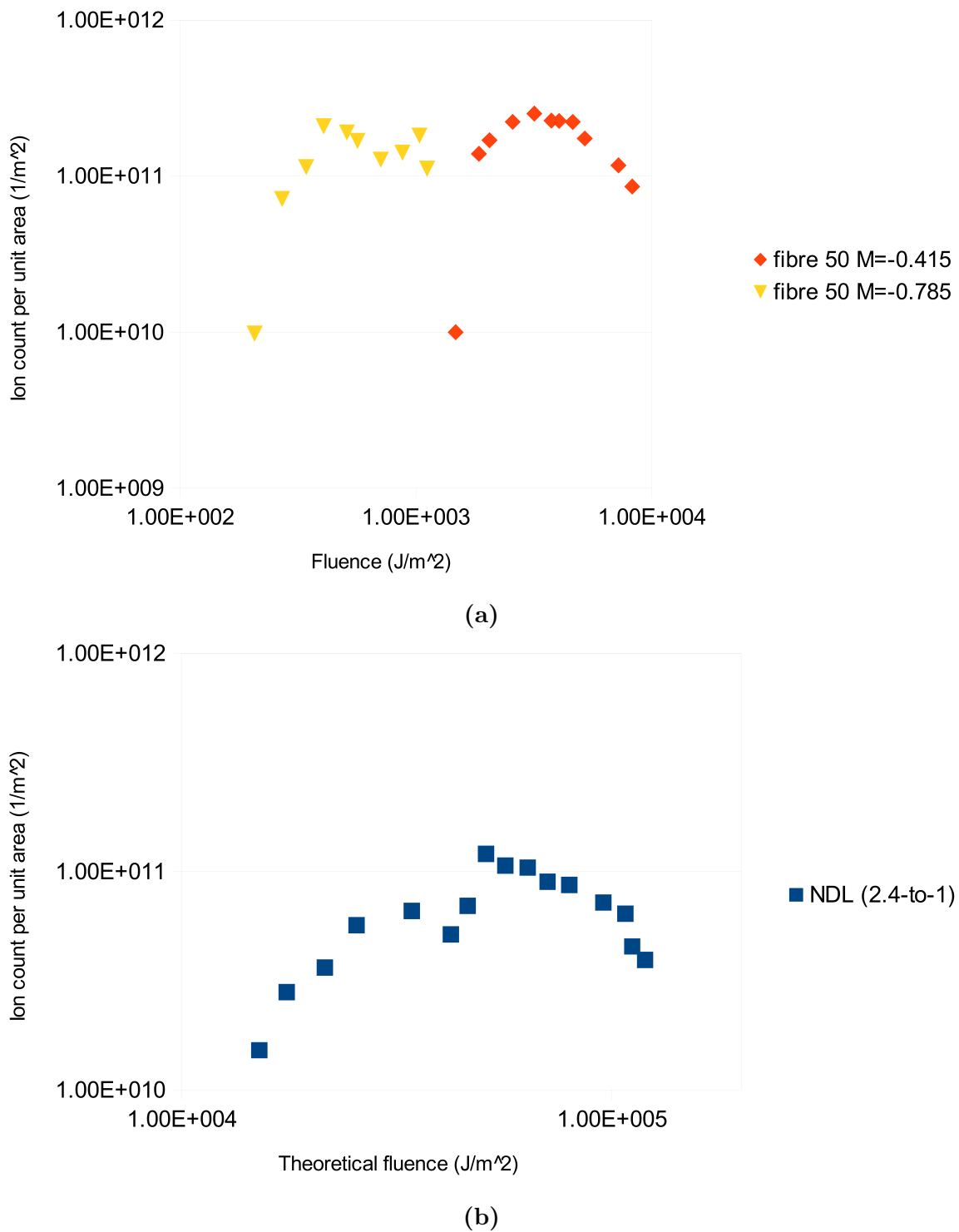


Figure 3.3: a) Sensitivity profiles for 50 μm fibre at 2.4-to-1 and 1.27-to-1 magnifications; b) sensitivity profile for 3–5 μm Gaussian-like spot for fibre-less configuration.

it does for Qiao's ion source configuration. As expected sensitivity increases with fluence at first as the sample is more efficiently consumed, but reaches an optimum and begins to decrease as the effective spot size increases and fragmentation effects dominate.

3.4 General discussion

The following suggestions can improve the experimental results and allow further investigations. The biggest issue is transmission loss inside the ion source. It needs to be resolved without sacrificing the geometry. Normal incidence of the laser beam produces the smallest possible spot. Due to a large gap between an ion transport cell and the target, the gas flow carries ions away from the entrance to the first quadrupole set. The gap needs to be sealed from the environment of the ion source and the seal needs to allow for free raster of the target.

The other big issue for this experiment is the competition of hysteresis with the ionization process. The use of hysteresis-resistant matrices might be necessary, however, there is a need to produce an even layer of matrix and analyte for a flat signal response during the raster. 2,5-dihydroxybenzoic acid (DHB) is a prime example of hysteresis-resistant matrix, but the spotting technique we employ applied to this matrix produces large matrix crystals with uneven analyte distribution. The usual use of DHB involves an active scanning for hot spots, where the signal rapidly increases. Unfortunately, not all of the DHB surface is evenly covered with such hot spots. A number of deposition techniques produce homogeneous deposition of matrix, but not all provide proper integration of the analyte inside the matrix crystal. DHB deposition via pneumatic system or sublimation can produce even films and small crystals, but do not integrate analyte properly, leading to a decreased ionization efficiencies.

Another suggestion includes the use of halogen-substituted matrices such as 4-chloro- α -cyanocinnamic acid. The addition of halogen reduces the overall proton

affinity of the matrix by pooling an electron from π -region [80], leading to a lower analyte suppression, smaller number of clusters and improved signal-to-noise ratio [81]. Halogenated matrices are deemed for use with small proton affinities, low quantity and high hydrophobicity analytes, although they do not provide any advantage over α -cyano-4-hydroxycinnamic acid for very basic samples.

3.5 Conclusion

The results discussed in previous sections form a foundation for further investigations for sensitivity in MALDI. Smaller spots at higher fluences for fibre and fibre-less configurations seem to produce higher sensitivity than in larger spots. Improved sensitivity benefits dynamic range in MALDI imaging, even if the lateral resolution is limited by other factors. A practical method of using smaller spots without increasing acquisition time is needed.

Sensitivity profile for Gaussian-like beam for sub 10 μm spot construction shows trends similar to fibre beams of larger sizes, although the absolute sensitivity measurements are limited due to ion loss in the ion source.

Bibliography

- [1] HM Fales, GW Milne, JJ Pisano, HB Brewer, MS Blum, JG MacConnell, J Brand, and N Law. Biological applications of electron ionization and chemical ionization mass spectrometry. *Recent Progress in Hormone Research*, 28:591, 1972.
- [2] HD Beckey. Field ionization mass spectrometry. *Research/Development*, 20:26, 1969.
- [3] U Boesl, R Weinkauf, C Weickhardt, and EW Schlag. Laser ion sources for time-of-flight mass spectrometry. *Journal of Mass Spectrometry and Ion Processes*, 131:87, 1993.
- [4] DR Kearns and M Calvin. Solid state ionization potentials of some aromatic organic compounds. *Journal of Chemical Physics*, 34:2026, 1960.
- [5] F Hillenkamp, E Unsöld, F Kaufmann, and R Nitsche. Laser microprobe mass analysis of organic materials. *Nature*, 256:119, 1975.
- [6] RD Macfarlane and DF Torgerson. Californium-252 plasma desorption mass spectrometry. *Science*, 191:920, 1976.
- [7] HR Morris, M Panico, M Barber, RS Bordoli, RD Sedwick, and A Tyler. Fast atom bombardment: a new mass spectrometric method for peptide sequence analysis. *Biochemical and Biophysical Research Communications*, 101:623, 1981.

- [8] The Nobel Prize in Chemistry 2002. http://www.nobelprize.org/nobel_prizes/chemistry/laureates/2002/. Accessed: 2013-09-12.
- [9] AE Cameron and DF Eggers. An ion "velocitron". *Reviews of Scientific Instruments*, 19:605, 1948.
- [10] C Weickhardt, F Moritz, and J Grotemeyer. Time-of-flight mass spectrometry: state-of-the-art in chemical analysis and molecular science. *Mass Spectrometry Reviews*, 15:139, 1996.
- [11] WC Wiley and IH McLaren. Time of flight mass spectrometer with improved resolution. *Reviews of Scientific Instruments*, 26:1150, 1955.
- [12] BA Mamyrin, VI Karataev, DV Shmikk, and VA Zagulin. The mass-reflectron, a new nonmagnetic time-of-flight mass spectrometer with high resolution. *Soviet Physics, JETP*, 37:45, 1973.
- [13] BA Mamyrin. Time-of-flight mass spectrometry (concepts, achievements, and prospects). *International Journal of Mass Spectrometry and Ion Processes*, 206:251, 2001.
- [14] BA Mamyrin. Laser assisted reflectron time-of-flight mass spectrometry. *International Journal of Mass Spectrometry and Ion Processes*, 131:1, 1994.
- [15] GJ O'Halloran, GJ Fluegge, JF Betts, and WL Everett. *Technical Documentary Report ASD-TDR-62-644, Part I and II*. Research Laboratory Division, Southfield, Michigan, 1964.
- [16] OA Mirgorodskaya, AA Shevchenko, IV Chernushevish, AF Dodonov, and AI Miroshnikov. Electrospray ionisation time-of-flight mass spectrometry in protein chemistry. *Analytical Chemistry*, 66:99, 1994.
- [17] JHJ Dawson and M Guilhaus. Orthogonal-acceleration time-of-flight mass spectrometer. *Rapid Communications in Mass Spectrometry*, 3:155, 1989.

- [18] AN Krutchinsky, IV Chernushevich, VL Spicer, W Ens, and KG Standing. Collisional damping interface for an electrospray ionization time-of-flight mass spectrometer. *Journal of the American Society for Mass Spectrometry*, 9:569, 1998.
- [19] AN Krutchinsky, AV Loboda, VL Spicer, R Dworschak, W Ens, and KG Standing. Orthogonal injection of matrix-assisted laser desorption/ionization ions into a time-of-flight spectrometer through a collisional damping interface. *Rapid Communications in Mass Spectrometry*, 12:508, 1998.
- [20] W Paul and H Steinwedel. A new mass spectrometry without magnetic field. *Journal of Natural Research A*, 8:448, 1953.
- [21] The Nobel Prize in Physics 1989. http://www.nobelprize.org/nobel_prizes/physics/laureates/1989/. Accessed: 2013-09-18.
- [22] RE March and RJ Hughes. *Quadrupole storage mass spectrometry*. John Wiley and Sons: New York, 1989.
- [23] AK Shukla and JH Futrell. Dissociation of ions by collisional activation. *Journal of Mass Spectrometry*, 35:1069, 2000.
- [24] RA Yost and CG Enke. Selected ion fragmentation with a tandem quadrupole mass spectrometer. *Journal of American Chemical Society*, 100:2274, 1978.
- [25] GL Glish and DE Goeringer. Tandem quadrupole/time-of-flight instrument for mass spectrometry/mass spectrometry. *Analytical Chemistry*, 56:2291, 1984.
- [26] HJ Xu, M Wada, J Tanaka, H Kawakami, I Katayama, and S Ohtani. A new cooling and focusing device for ion source. *Nuclear Instruments and Methods in Physics*, 333:274, 1993.
- [27] M Yamashita and JB Fenn. Electrospray ion source. Another variation on the free-jet theme. *Physical Chemistry*, 88:4451, 1984.

- [28] JB Fenn, M Mann, CK Meng, VN Wong, and CM Whitehouse. Electrospray ionisation for mass spectrometry of large biomolecules. *Science*, 246:64, 1989.
- [29] K Tanaka, H Waki, Y Ido, S Akita, Y Yoshida, and T Yoshida. Protein and polymer analysis up to m/z 100,000 by laser ionisation time-of-flight mass spectrometry. *Rapid Communication in Mass Spectrometry*, 2:151, 1988.
- [30] M Karas, D Bachmann, and F Hillenkamp. Influence of the wavelength in high-irradiance ultraviolet laser desorption mass spectrometry of organic molecules. *Analytical Chemistry*, 57:2935, 1985.
- [31] M Karas and F Hillenkamp. Laser desorption ionisation of proteins with molecular masses exceeding 10,000 daltons. *Analytical Chemistry*, 60:2299, 1988.
- [32] RC Beavis and BT Chait. Cinnamic acid derivatives as matrices for ultraviolet laser desorption mass spectrometry of proteins. *Rapid Communication in Mass Spectrometry*, 12:432, 1989.
- [33] K Strupat, M Karas, and F Hillenkamp. 2,5-dihydroxybenzoic acid: a new matrix for laser desorption-ionization mass spectrometry. *International Journal of Mass Spectrometry Ion Processes*, 72:89, 1991.
- [34] RC Beavis, T Chaudhary, and BT Chait. Alpha-cyano-4-hydroxycinnamic acid as a matrix for matrix-assisted laser desorption mass spectrometry. *Organic Mass Spectrometry*, 27:156, 1992.
- [35] J Soltwisch, TW Jaskolla, F Hillenkamp, M Karas, and Dresisewerd. Ion yields in UV-MALDI mass spectrometry as a function of excitation laser wavelength and optical and physico-chemical properties of classical and halogen-substituted MALDI matrices. *Analytical Chemistry*, 84:6567, 2012.

- [36] P Demirev, A Westma, CT Rimann, P Hakansson, D Barofsky, BUR Sundqvist, YD Chen, W Seibt, and K Siegbahn. Matrix-assisted laser desorption with ultra-short laser pulses. *Rapid Communications in Mass Spectrometry*, 6:187, 1992.
- [37] A Vertes, R Gijbels, and RD Levine. Homogeneous bottleneck model of matrix-assisted ultraviolet-laser desorption of large molecules. *Rapid Communications in Mass Spectrometry*, 4:228, 1990.
- [38] R Knochenmuss and LV Zhigilei. Molecular dynamics simulations of MALDI: laser fluence and pulse width dependence of plume characteristics and consequences for matrix and analyte ionization. *Journal of Mass Spectrometry*, 45:333, 2010.
- [39] RE Johnson. Models for matrix-assisted desorption by a laser-pulse. *International Journal of Mass Spectrometry and Ion Processes*, 139:25, 1994.
- [40] A Vogel and V Venugopalan. Mechanisms of pulsed laser ablation of biological tissues. *Chemical Reviews*, 103:2079, 2003.
- [41] W Zhang and BT Chait. Radial velocity distributions of molecular ions produced by matrix-assisted laser desorption/ionization. *International Journal of Mass Spectrometry and Ion Processes*, 160:259, 1998.
- [42] CD Mowry and MV Johnston. Internal energy of neutral molecules ejected by matrix-assisted laser desorption. *Journal of Physical Chemistry*, 98:1904, 1994.
- [43] R Knochenmuss and R Zenobi. MALDI ionization: the role of in-plume processes. *Chemical Reviews*, 103:441, 2003.
- [44] V Gabelica, E Schulz, and M Karas. Internal energy build-up in matrix-assisted laser desorption/ionization. *Journal of Mass Spectrometry*, 39:579, 2004.

- [45] A Verentchikov, I Smirnov, and M Vestal. Collisional cooling and ion formation processes in orthogonal MALDI at intermediate gas pressures. *Proceedings of the ASMS Conference on Mass Spectrometry and Allied Topics*, 1999.
- [46] M Karas and R Krüger. Ion formation in MALDI: the cluster ionization mechanism. *Chemical Reviews*, 103:427, 2003.
- [47] M Karas, M Glückmann, and J Schäer. Ionization in matrix-assisted laser desorption/ionization: singly charged molecular ions are lucky survivors. *Journal of Mass Spectrometry*, 35:1, 2000.
- [48] PD Setz and R Knochenmuss. Exciton mobility and trapping in a MALDI matrix. *Journal of Physical Chemistry*, 109:4030, 2005.
- [49] TW Jaskolla and M Karas. Using fluorescence dyes as a tool for analyzing the MALDI process. *Journal of American Society of Mass Spectrometry*, 19:1054, 2008.
- [50] R Zenobi and R Knochenmuss. Ion formation in MALDI mass spectrometry. *Mass Spectrometry reviews*, 17:337, 1998.
- [51] R Knochenmuss and LV Zhigilei. What determines MALDI ion yields? A molecular dynamics study of ion loss mechanisms. *Analytical and Bioanalytical Chemistry*, 402:2511, 2011.
- [52] TW Jaskolla and M Karas. Compelling evidence for lucky survivor and gas phase protonation: the unified MALDI analyte protonation mechanism. *Journal of American Society of Mass Spectrometry*, 22:976, 2011.
- [53] R Knochenmuss. Ion formation mechanisms in UV-MALDI. *Analyst*, 131:966, 2006.
- [54] P Chaurand, Schwartz SA, ML Reyzer, and RM Caprioli. Imaging mass spectrometry: principles and potentials. *Toxicologic Pathology*, 33:92, 2005.

- [55] A Bodzon-Kulakowska, A Drabik, J Ner, JH Kotlinska, and P Suder. Desorption electrospray ionization (desi) for beginners - how to adjust settings for tissue imaging. *Rapid Communication in Mass Spectrometry*, 28:1, 2014.
- [56] LA McDonnell and RMA Heeren. Imaging mass spectrometry. *Mass Spectrometry Reviews*, 26:606, 2007.
- [57] C Lechene, F Hillion, G McMahon, D Benson, AM Kleinfeld, JP Kampf, D Distel, Y Luyten, J Bonventre, D Hentschel, KM Park, S Ito, M Schwartz, G Benichou, and G Slodzian. High-resolution quantitative imaging of mammalian and bacterial cells using stable isotope mass spectrometry. *Journal of Biology*, 5:20, 2006.
- [58] SA Schwartz, ML Reyzer, and RM Caprioli. Direct tissue analysis using matrix-assisted laser desorption/ionization mass spectrometry: practical aspects of sample preparation. *Mass Spectrometry Reviews*, 38:699, 2003.
- [59] B Spengler and M Hubert. Scanning microprobe matrix-assisted laser desorption ionization (SMALDI) mass spectrometry - instrumentation for sub-micrometer resolved LDI and MALDI surface analysis. *Journal of the American Society of Mass Spectrometry*, 13:735, 2002.
- [60] A Zavalin, EM Todd, PD Rawhouser, JH Yang, JL Norris, and RM Caprioli. Direct imaging of single cells and tissue at sub-cellular spatial resolution using transmission geometry MALDI MS. *Journal of Mass Spectrometry*, 47:1473, 2012.
- [61] DA Allwood, RW Dreyfus, IK Perera, and PE Dyer. UV optical absorption of matrices used for matrix-assisted laser desorption/ionization. *Rapid Communications in Mass Spectrometry*, 10:1575, 1996.
- [62] A Holle, A Haase, M Kayser, and J Höhdorf. Optimizing UV laser focus profiles for improved MALDI performance. *Journal of Mass Spectrometry*, 41:705, 2006.

- [63] H Qiao, V Spicer, and W Ens. The effect of laser profile, fluence and spot size on sensitivity in orthogonal-injection matrix-assisted laser desorption/ionization time-of-flight mass spectrometry. *Rapid Communications in Mass Spectrometry*, 22:2779, 2008.
- [64] W Ens, Y Mao, F Mayer, and KG Standing. Properties of matrix-assisted laser desorption. Measurements with a time-to-digital converter. *Rapid Communications in Mass Spectrometry*, 5:117, 1991.
- [65] K Dreiswerd, M Schürenberg, M Karas, and F Hillenkamp. Influence of the laser intensity and spot size on the desorption of molecules and ions in matrix-assisted laser desorption ionization with a uniform beam profile. *International Journal of Mass Spectrometry and Ion Processes*, 141:127, 1995.
- [66] G Westmacott, W Ens, F Hillenkamp, K Dreiswerd, and M Schürenberg. The influence of the laser fluence on ion yield in matrix-assisted laser desorption ionization mass spectrometry. *International Journal of Mass Spectrometry*, 221:67, 2002.
- [67] S Guenther, M Koestler, O Schulz, and B Spengler. Laser spot size and laser power dependence of ion formation in high resolution MALDI imaging. *Analytical Chemistry*, 294:7, 2010.
- [68] VM Doroshenko, VV Laiko, NI Taranenko, VD Berkout, and HS Lee. Recent developments in atmospheric pressure MALDI mass spectrometry. *International Journal of Mass Spectrometry*, 72:652, 2002.
- [69] AV Loboda, S Ackloo, and IV Chernushevich. A high-performance matrix-assisted laser desorption/ionization orthogonal time-of-flight mass spectrometer with collisional cooling. *Rapid Communications in Mass Spectrometry*, 17:2508, 2003.

- [70] A Loboda, A Krutchinsky, O Loboda, J McNabb, V Spicer, W Ens, and K Standing. Novel linac II electrode geometry for creating an axial field in a multipole ion guide. *European Journal of Mass Spectrometry*, 6:531, 2000.
- [71] RW Hosken. Circle of least confusion of a spherical reflector. *Applied Optics*, 46:3107, 2007.
- [72] LV Zhigilei and BJ Garrison. Microscopic mechanisms of laser ablation of organic solids in the thermal and stress confinement irradiation regimes. *Journal of Applied Physics*, 88:1281, 2000.
- [73] AF Dodonov, AV Loboda, VI Kozlovski, IV Soulimenkov, VV Raznikov, Z Zhou, T Howarth, and H Wollnik. High-resolution electrospray ionization orthogonal-injection time-of-flight mass spectrometer. *European Journal of Mass Spectrometry*, 6:481, 2000.
- [74] SL Cohen and BT Chait. Influence of matrix solution conditions on the MALDI-MS analysis of peptides and proteins. *Analytical Chemistry*, 68:31, 1996.
- [75] V Horneffer, A Forsmann, K Strupat, F Hillenkamp, and U Kubitschek. Localization of analyte molecules in MALDI preparations by confocal laser scanning microscopy. *Analytical Chemistry*, 73:1016, 2001.
- [76] H Wei, K Nolkrantz, DH Powell, JH Woods, MC Ko, and RT Kennedy. Electrospray sample deposition for matrix-assisted laser desorption/ionization (MALDI) and atmospheric pressure MALDI mass spectrometry with attomole detection limits. *Rapid Communication in Mass Spectrometry*, 18:1193, 2004.
- [77] DA Allwood, IK Perera, J Perkins, PE Dyer, and GA Oldershaw. Preparation of near homogeneous samples for the analysis of matrix-assisted laser desorption/ionization processes. *Applied Surface Science*, 103:231, 1996.

- [78] T Porta, R Grivet, C Knochenmuss, E Varesio, and G Hopfgartner. Alternative CHCA-based matrices for the analysis of low molecular weight compounds by UV-MALDI-tandem mass spectrometry. *Journal of Mass Spectrometry*, 46:144, 2011.
- [79] I Fournier, RC Beavis, JC Blais, JC Tabet, and G Bolbach. Hysteresis effects observed in MALDI using oriented, protein-doped matrix crystals. *International Journal of Mass Spectrometry and Ion Processes*, 169/170:19, 1997.
- [80] J Soltwisch, TW Jaskolla, F Hillenkamp, M Karas, and K Dreisewerd. Ion yields in UV-MALDI mass spectrometry as a function of excitation laser wavelength and optical and physico-chemical properties of classical and halogen-substituted MALDI matrixes. *Analytical Chemistry*, 84:6567, 2012.
- [81] TW Jaskolla, WD Lehmann, and M Karas. 4-Chloro-alpha-cyanocinnamic acid is an advanced, rationally designed MALDI matrix. *Proceedings of the National Academy of Sciences*, 105:12200, 2008.